

Structural determinants of voltage-gating properties in calcium channels

Monica L. Fernández-Quintero^{1,2,§} ([0000-0002-6811-6283](#)), Yousra El Ghaleb^{1,§} ([0000-0002-0829-5865](#)), Petronel Tuluc³ ([0000-0003-3660-6138](#)), Marta Campiglio¹ ([0000-0002-9629-2073](#)), Klaus R. Liedl² ([0000-0002-0985-2299](#)), and Bernhard E. Flucher^{1*} ([0000-0002-5255-4705](#))

¹ Department of Physiology and Medical Physics, Institute of Physiology, Medical University Innsbruck, Innsbruck, Austria

² Institute of General, Inorganic and Theoretical Chemistry, and Center for Molecular Biosciences Innsbruck (CMBI), University of Innsbruck, Innsbruck, Austria.

³ Department of Pharmacology and Toxicology, Institute of Pharmacy and Center for Molecular Biosciences, University of Innsbruck, Innsbruck, Austria

[§] These authors contributed equally to the work

* Corresponding Author:

Bernhard E. Flucher, PhD
Department of Physiology and Medical Physics
Medical University Innsbruck
Schöpfstraße 41
A-6020 Innsbruck, Austria
Phone: +43 512 9003 70836
Email: bernhard.e.flucher@i-med.ac.at

Keywords

Voltage-gated calcium channel, Ca_v1.1, voltage-sensing, resting-state structure, molecular dynamics simulation

31

32 **Abstract**

33 Voltage-gated calcium channels control key functions of excitable cells, like synaptic transmission in
34 neurons and the contraction of heart and skeletal muscles. To accomplish such diverse functions,
35 different calcium channels activate at different voltages and with distinct kinetics. To identify the
36 molecular mechanisms governing specific voltage-sensing properties we combined structure
37 modeling, mutagenesis, and electrophysiology to analyze the structures, free energy, and transition
38 kinetics of the activated and resting states of two functionally distinct voltage-sensing domains
39 (VSDs) of the eukaryotic calcium channel $\text{Ca}_v1.1$. Both VSDs displayed the typical features of the
40 sliding helix model; however, they greatly differed in ion-pair formation of the outer gating charges.
41 Specifically, stabilization of the activated state enhanced the voltage-dependence of activation, while
42 stabilization of resting states slowed the kinetics. This mechanism provides a mechanistic model
43 explaining how specific ion-pair formation in separate VSDs can realize the characteristic gating
44 properties of voltage-gated cation channels.

45

Introduction

Voltage-gated calcium channels (Ca_v) translate membrane depolarization into calcium influx. Thus, they contribute to cellular excitability and they couple electrical activity to fundamental cell functions like contraction of heart and skeletal muscle, secretion of neurotransmitters and hormones, and the regulation of gene expression. Together with voltage-gated sodium channels (Na_v), Ca_v s form a structurally related ion channel superfamily with a four-fold symmetry (Fig. 1A). Their pore-forming α_1 subunits are composed of four homologous but non-identical domains (repeats I-IV), each containing six trans-membrane helices (S1-S6). The S5 and S6 helices plus the connecting P loop of all four repeats form the central channel pore with the selectivity filter and the activation gate (Catterall et al., 2020). Helices S1-S4 of each repeat form separate voltage-sensing domains (VSD). The S4 helix contains positively charged residues (termed gating charges) in every third position, and its movement across the electric field upon membrane depolarization is thought to initiate the conformational change resulting in channel opening (Catterall et al., 2017).

Several high-resolution structures of prokaryotic and eukaryotic Na_v channels have been solved (Lenaus et al., 2017; Pan et al., 2018; Payandeh et al., 2011; Yan et al., 2017; Zhang et al., 2012). Recent advances in cryo-electron microscopy (cryo-EM) enabled the determination of the structure of the voltage-gated calcium channel $\text{Ca}_v1.1$ at 3.6 Å resolution, displaying a closed pore and the VSDs in the activated up-state (Wu et al., 2016, 2015). Very recently three cryo-EM structures of homo-tetrameric sodium channels experimentally locked in resting- (or VSD-down) states have been reported (Wisedchaisri et al., 2021, 2019; Xu et al., 2019). However, up to now the resting states of eukaryotic Ca_v and Na_v channels remained inaccessible to experimental structure determination. Nevertheless, many years of experimental work and structure modeling provide ample support for the sliding helix model of the voltage-sensor action (Catterall et al., 2017; Yarov-Yarovoy et al., 2012). According to this model the negative membrane potential at rest pulls the positively charged S4 helices down toward the cytoplasmic side of the membrane holding the channel gate closed. The reversal of the electric field upon membrane depolarization causes the outward displacement of the S4 helix by about 10 Å. The movement of 2 to 3 positive gating charges through the hydrophobic constriction site (HCS) in the center of the VSD is facilitated by the transient formation of ion-pair interactions with negative counter charges in the other helices of the VSD (Catterall et al., 2017).

While this model describes the principal mode of voltage-sensor action, without further structure-function data it does not explain how the four homologous, but structurally distinct VSDs of eukaryotic channels cooperate in channel gating and how the unique gating properties of different channel isoforms are achieved. The distinct structure of the four VSDs of eukaryotic Na_v and Ca_v suggests that there might be considerable variability between the four VSDs of a channel in the

movement of the S4 helices and the molecular interactions of their gating charges. In fact, accumulating evidence indicates functional differences between the VSDs of individual channel isoforms (Ahern et al., 2016; Pantazis et al., 2014; Tuluc et al., 2016a). The rabbit skeletal muscle $\text{Ca}_v1.1$ is the first member of the Ca_v family for which the structure has been solved (Wu et al., 2016, 2015; Zhao et al., 2019). Biophysically it is characterized by slow kinetics and right-shifted voltage-dependence of activation (Tuluc et al., 2016a). Together these attributes make $\text{Ca}_v1.1$ a prime candidate for studying how specific structural features of the VSDs determine voltage-dependence and kinetics of channel activation.

Here we applied molecular dynamics (MD) simulation and Markov state modeling (MSM) combined with site-directed mutagenesis and electrophysiological analyses to identify the molecular mechanism by which individual VSDs determine the characteristic voltage-dependence and kinetics of current activation. Our structure models of the activated and resting states of $\text{Ca}_v1.1$ VSDs I and IV are consistent with the sliding helix model and yielded reliable predictions of the importance of ion-pair formation between the outer gating charges and various counter charges within the particular VSD. Our data provide novel insight in how the stabilization of the VSDs in resting and/or the activated states shapes the kinetics and voltage-dependence of activation, respectively.

Results

The structure of $\text{Ca}_v1.1$ reveals differences between VSDs

Based on the cryo-EM structure of $\text{Ca}_v1.1$ (Wu et al., 2016, 2015) we generated a new structural model to study the molecular mechanisms determining the specific gating properties of this voltage-gated calcium channel. To this end we used the *Rosetta* computational modeling software (Bender et al., 2016; Rohl et al., 2004) to build a homology model of the human eukaryotic $\text{Ca}_v1.1$ and included all missing loops and modelled both splice variants with and without exon 29 (Tuluc et al., 2009). The resulting models were equilibrated and simulated at 300 K in the membrane environment to identify favorable side-chain orientations and to relax the protein.

$\text{Ca}_v1.1$ is a pseudo-tetrameric channel with a domain-swapped arrangement in which each VSD (S1-S4) is positioned next to the pore domain (PD; S5-S6) of the adjacent repeat in a clock-wise orientation (Catterall et al., 2017) (Fig. 1B,D). The structures of the individual repeats closely resemble the crystal structure of Na_vAb (C α RMSD of 2.7 Å) (Payandeh et al., 2011), which is regarded as phylogenetic ancestor of Ca_v and Na_v channels and for which considerable structural information is available (Fig. 1E; Fig. 1-figure supplement 1). While all four VSDs of $\text{Ca}_v1.1$ display the canonical voltage-sensor fold, individually they differ from one another in significant aspects like the

length of the helical structures and the number of gating charges in S4 (Fig. 1-figure supplement 2). Only VSD IV contains four gating charges (R1-R4) at the three-residue interval, like Na_vAb (Fig. 1C). VSDs I and III possess an additional positive charge (K0) at the outer end of S4, and VSD II an additional gating charge (K5) at the cytoplasmic side of S4. All four VSDs are in the activated (S4-up) state in that (K0) R1, R2, and R3 are positioned above the phenylalanine (in S2) of the HCS and R4 (and K5) below (Fig. 1F).

As predicted by the sliding helix model (Catterall et al., 2017), the gating charges form ion-pairs with counter charges of the extracellular negative cluster (ENC) and intracellular negative cluster (INC). The interactions of the inner gating charges with countercharges of the INC are identical in the four VSDs of Ca_v1.1, representing the typical arrangement of the highly conserved charge-transfer center (Tao et al., 2010). However, between the VSDs the outer ion-pair interactions differ. Overall, the four VSDs of Ca_v1.1 can be grouped in two classes – VSDs I and III, and VSDs II and IV, respectively – each with the same number and position of counter charges in the ENC. While in VSD I and VSD III the gating charges form ion-pairs with two glutamate residues in the S2 helix, VSD II and VSD IV gating charges interact with one negative countercharge each in the S2 and S3 helices. Also, in VSD I and VSD III the additional outermost gating charges are lysines (K0), whereas in VSD II and VSD IV the innermost gating charge is a lysine residue (K4) instead of an arginine (R4) in VSD I and VSD III. Note that lysine forms only a single interaction with a negative countercharge in the INC as opposed to two formed by arginine. Together these differences in the ion-pairs formed by the gating charges indicates that the activated state of VSDs I and III is considerably more stabilized than that of VSDs II and IV.

MD simulation and MSM of VSD I in activated and resting states

The interactions between gating charges and their ion-pair partners observed in the structure model based on available cryo-EM structures of Ca_v1.1 merely represent a snapshot depicting the endpoint of the voltage-sensing process. However, because high-resolution structures of resting states of Ca_v channels are lacking, the molecular details of the steps leading up to VSD activation are still elusive. Exploiting the potential of structure modeling to fill this gap (Jensen et al., 2012; Yarov-Yarovoy et al., 2012), we applied molecular dynamics (MD) simulation and Markov state modeling (MSM) of individual VSDs to predict the structures, kinetics, and energy levels of resting states. To overcome the high energy barriers and the timescale limitations of MD simulations in the absence of the membrane potential, we used *Umbrella* sampling. This enhanced sampling technique explores the conformational transitions of a VSD as the positively charged S4 helix moves along the likely pathway towards the cytoplasmic side of the VSD, and thus create the seeding points for subsequent MD simulations. For this purpose, the obtained structures were clustered based on a geometrical RMSD

147 criterion resulting in about 50 cluster representatives. These were simulated for 100 ns each
148 (aggregated simulation time close to 5 μ s) to obtain unbiased trajectories, which were then projected
149 in a TICA, representing the slowest reaction coordinates. Finally, the kinetic coordinate system
150 provided by the TICA allows calculation of thermodynamics and kinetics by a MSM (Fig. 2-figure
151 supplement 1).

152 Using this approach, we modeled the resting state structures of $\text{Ca}_v1.1$ VSD I and VSD IV, because
153 they represent the two structurally distinguishable classes of VSDs (see Fig. 1F; Fig. 1-figure
154 supplement 2), and because they differentially regulate the specific gating properties of skeletal
155 muscle calcium currents. VSD I determines $\text{Ca}_v1.1$'s slow activation kinetics and VSD IV its voltage-
156 dependence of activation (Nakai et al., 1994; Tuluc et al., 2016a). The latter is regulated by
157 alternative splicing in that exclusion of the 19 amino acids of exon 29 from the extracellular loop
158 linking IVS3 and S4 causes a 30 mV left-shift of the voltage-dependence of activation and a several-
159 fold increase in current density (Tuluc et al., 2009). Previously we demonstrated that the loss of
160 voltage sensitivity upon insertion of exon 29 is caused by the relative lateral displacement of S3 and
161 S4 and the resulting loss of ionic interactions of the outer gating charges (R1, R2) with a single
162 counter charge (D1196) in the S3 helix (Tuluc et al., 2016b). Considering the importance of these
163 ionic interactions in VSD IV for regulating the channel's voltage-dependence we hypothesized that
164 similarly the specific kinetic properties of $\text{Ca}_v1.1$ may be encoded in the structure, ionic interactions,
165 and the molecular kinetics of the state transitions of VSD I.

166 The free energy maps calculated for the MD simulation of VSD I, VSD IVe, and VSD IVa each
167 comprised four energy minima (Fig. 2A,E,I) and the corresponding structures resembled the activated
168 and three resting states, as predicted by the sliding helix model. Across these states the S4 helix of
169 VSD I described a stepwise downward movement of 15.3 Å, corresponding to 3 helical turns (Fig.
170 2B,C). In the activated state the gating charges K0, R1, R2, and R3 were above phenylalanine (F97) of
171 the HCS, and only R4 was below it. In the deepest resting state 1 only K0 and R1 were positioned
172 above the HCS, while R2, R3, and R4 were located below it. In all four states IS4 adopted a shifting
173 stretch of 3_{10} -helical conformation (Fig. 2-figure supplement 2), so that the side chains of the gating
174 charges all pointed towards the center of the VSD. As IS4 moved from the activated state to resting
175 state 1, R4, R3, R2, and R1 sequentially formed ion-pairs with counter charges of the INC (E100 in IS2,
176 and D126 in IS3), which are part of the highly conserved charge transfer center of voltage-gated
177 cation channels (Fig. 2B; Fig 3A) (Tao et al., 2010). In all states also the gating charges above and
178 below the HCS formed extensive ionic bonds with negative counter charges in IS1 and IS2. In the
179 resting states 2 and 3 and in the activated state R1, R2, and R3 formed ion bonds with E87 and E90,
180 plus in resting state 3 and the activated state K0 formed an additional ion bond with E76 in the IS1-S2

loop. In resting states 1 and 2 gating charges R3 and R4 formed ion bonds with E49 and E54 at the cytoplasmic end of IS1. This multitude of ionic interactions stabilizes each of the consecutive states and thus strictly delineates the path of S4 through VSD I upon channel activation and deactivation. Note that in addition to the indicated ionic bonds, the gating charges form transient hydrogen bonds and hydrophobic and polar interactions with several other putative interaction partners, all of which might contribute to the movement of S4 across the membrane electrical field, but are not subject of the present study.

Next, we used Markov state modeling (MSM) of the MD simulation data to estimate transition times between the resting and activated states during the activating and deactivating VSD motion (Fig. 2B,D; Fig. 2-figure supplement 3; Supplementary file 1 – Table 1). The conformational transitions between the different activation states of Ca_v1.1 VSD I occurred in the high μ s to low millisecond timescale. Because the values calculated in our model are obtained in the absence of the force provided by changes in the electric field, the absolute transition times derived from MSM may not correspond to the actual transition times of the VSD upon physiological activation and deactivation. Nevertheless, relative differences between transition times provide meaningful information when compared between different VSDs or functionally different mutants (see below). Relying on a simple transition state theory model (Laidler and King, 1983) we generated a schematic 1D-representation of the high-dimensional free energy surface (Fig. 2D), allowing an intuitive interpretation of free energy levels of the states and ΔG of the energy barriers. The free energy of the activated state was the lowest and transitions in the activating direction were two- to four-times faster than in the deactivating direction, consistent with the fact that our MD simulations were performed on structure models at a depolarized membrane (0 mV), which favors the activated state of the VSDs. The energy barriers (ΔG) for the three state transitions of VSD I in the activating direction were between 48 and 51 kJ/mol.

MD simulation and MSM of VSD IV in activated and resting states

How do the molecular interactions during VSD activation and deactivation and the kinetics of state transition differ between VSD I and VSD IV to explain their distinct functions in determining kinetics and voltage-dependence of activation, respectively? (Tuluc et al., 2009) The basic structural features of the activated and resting states of VSD IV corresponded to those of VSD I, except that in VSD IV the translocation of S4 across the HCS covered a shorter distance and involved fewer ion-pair interactions (Fig. 2F,G,J,K). Upon the deactivating motion of the S4 helix of VSD IV only a single gating charge (R3) fully translocated from a position above the HCS (F1161) to below it. Accordingly, the total vertical displacement in the two splice variants of IVS4 was 12.9 Å in VSD IVe and only 10.2 Å in VSD IVa, corresponding to roughly 2 helical turns.

In the four states of both VSD IV variants only the two inner gating charges R3 and K4 sequentially interacted with the conserved ion-pair partners of the charge transfer center (E1164 and D1186) (Fig. 2F,J; Fig 3A). R2 moved into the HCS but did not form ion-pairs with E1164 or D1186. In the deep resting states an additional ion-pair was formed between K4 and E1121 at the cytoplasmic end of IVS1. At variance with VSD I, ion-pair formation of the outer gating charges of VSD IV was completely absent in the resting states. Instead, R1 and R2 established several weaker hydrogen bonds with side chains of uncharged polar amino acids. In VSD IV ion-pair interactions of R1 and R2 with the ENC were limited to the activated state of the Ca_v1.1e splice variant. Within VSD IV they were established with a single ion-pair partner (D1196), the functional importance of which for splicing-dependent regulation of the voltage-dependence of activation had been shown previously (Tuluc et al., 2016b). Consistent with that study these interactions were greatly attenuated when exon 29 was included in the IVS3-S4 linker of Ca_v1.1a (Fig. 3A,C). The activated state structure of VSD IVa (containing exon 29) showed only a single H-bond between R2 and D1196, compared to two each of R1 and R2 with D1196 in VSD IVe (lacking exon 29). Thus, the three resting states of VSD IV are not stabilized by ion-pairs formed by the outer gating charges, and the ion-pairs forming in the activated state are further reduced by inclusion of exon 29 in the linker separating the two participating helices.

Can these striking structural differences explain the kinetic differences conferred to the channel by VSD I and IV? Our MSM calculations of state transition kinetics strongly support this notion. Compared to VSD I the energy barriers between the states were substantially lower in VSD IV (35-38 kJ/mol for IVe, and 35 to 42 kJ/mol for IVa) (Fig. 2H,L). Consistent with the differences in activation kinetics, the transition times determined for VSD IV were in the μ s range (Fig. 2F,J), which is two to three orders of magnitude faster than those of VSD I. Also, the transitions between resting states 1 and 2, and between resting state 3 and the activated state were about three times faster in Ca_v1.1a compared to Ca_v1.1e, indicating an effect of exon 29 insertion on the kinetics of VSD IV movement. However, compared to the substantial difference between the kinetically distinct VSD I and VSD IV, the differences in energy barriers and transition times between the two VSD IV splice variants remain unexpectedly small. Apparently, the calculated transition times primarily reflect differences in kinetics, but much less differences of the voltage-dependence of activation. This makes sense, considering that the height of energy barriers and the transition kinetics are expected to affect the sequential transitions of a VSD through all four states, which determine the channel activation kinetics, whereas changes in voltage-sensitivity primarily rely on the stabilization of the activated state and therefore are little affected by differences of the state transitions.

The direct comparison of VSD I and the two splice variants of VSD IV in the activated and resting states demonstrates striking differences between VSD I and IV in the extent of ion-pair formation in

the ENC (Fig. 3). As shown above, in VSD IV these involve interactions of R1 and R2 with the ion-pair partner D1196 in IVS3 formed in the activated state that are subject to modulation by alternative splicing of exon 29. VSD I lacks an analogous ion-pair partner in the corresponding position of IS3. Instead IS4 displays extensive ion-pairs with counter charges (E76, E87, E90) in IS2 that are sequentially formed by gating charges R3, R2, R1, and K0 in the activated and the intermediate resting states 2 and 3 (Video 1). This indicates that in VSDs I and IV the gating charges above the HCS utilize structurally distinct ion-pair partners to stabilize the voltage sensor either only in the activated state (VSD IV) or in the activated and resting states (VSD I). The additionally formed ion-pairs in the resting states of VSD I are paralleled by a remarkable increase in the energy barriers and the state transition times, suggesting that the number and strength of interactions between the gating charges and the ENC transiently formed in the resting states determine the slow activation kinetics of VSD I.

VSD I ion-pairs differentially regulate gating properties

To experimentally test this hypothesis, we simultaneously mutated both counter charges, E87 and E90, to alanine (E87A/E90A) in the rabbit GFP-Ca_v1.1e (Tanabe et al., 1988; Tuluc et al., 2009), expressed them in their native environment in dysgenic myotubes and examined the effects on the gating properties of its calcium currents (Fig. 4A). The structure of the VSDs in general and in particular the studied residues are highly conserved in Ca_v channels (Wu et al., 2016). Immunofluorescence labeling demonstrated that wildtype and mutant channels were equally expressed and targeted to triad junctions in the myotubes (Fig. 4-figure supplement 1). In contrast, their gating properties differed significantly (Fig. 4B-I; Supplementary file 1 - Table 2). As hypothesized, activation kinetics was more than four times faster in the mutant compared to wildtype (Fig. 4D,E), thus identifying E87 and/or E90 as critical determinants of the slow activation kinetics of Ca_v1.1. Interestingly, also the voltage-dependence of activation was right-shifted to more depolarizing potentials by 18.2 mV and the peak current density was somewhat reduced (Fig. 4F-I).

If the comparably long transition times for wildtype VSD I determined by MSM related to the experimentally determined activation kinetics, then MSM of the E87A/E90A mutant channel should result in rapid transition times. This was indeed the case! The transition times of VSD I on activation and deactivation of the E87A/E90A mutant were more than 50 times faster than those of the wildtype VSD (Fig. 4J-L; Fig. 2-figure supplement 3, Fig. 4-figure supplement 2, Supplementary file 1 - Tables 1 and 2; Videos 1 and 2). This supports our interpretation of the role of the two counter charges in determining the gating properties, and also substantiates the reliability and predictive value of the kinetic analysis of our MD simulations. Yet, it is worth noting that the transition kinetics derived from our MD simulation relate to the activation of an isolated VSD, whereas kinetics and voltage-dependence of channel activation reflect the concerted action of all four VSDs and its

mechanical transduction to the channel gate. Consequently, changes in activation properties of a single VSD will only result in similar changes of current activation, when this VSD is obligatory and rate-limiting for gating, or, in an allosteric model, according to its relative contribution to the gating process. This limitation may also account for the different magnitudes of the effects (50-fold vs. 5-fold) on the activation kinetics of the E87A/E90A mutant observed in MSM and current recordings.

As E87 and/or E90 govern the kinetics as well as voltage-dependence of $\text{Ca}_v1.1$ activation, we wondered whether these two properties are mechanistically linked to each other or separable? Our structural model predicts that E87 interacts with R1 in resting state 3, and with R1 and R2 in the activated state (Fig. 5A), which is consistent with a prime role in stabilizing the activated state. In contrast, E90 forms consecutive interactions with R3, R2, and R1 in resting state 2, resting state 3, and the activated state, respectively (Fig. 5K), thus stabilizing VSD I both in its resting and activated states. To examine the individual contributions of E87 and E90 to shaping the gating properties we generated constructs with individual E87A and E90A substitutions. The two mutations showed differential effects on the gating properties of $\text{Ca}_v1.1$ currents. The E87A mutation right-shifted the voltage-dependence of activation by 12.3 mV, while activation kinetics were not altered (Fig. 5B-G). In contrast, the E90A mutation accelerated the activation kinetics 4 to 5-fold and showed a 7.7 mV right-shift of voltage-dependence (Fig. 5L-Q).

Again, MD simulation and MSM analysis reflected these differential functional effects. In accordance with its effect on activation kinetics the E90A mutation, but not E87A, showed greatly accelerated transition times and reduced energy barriers between the resting and activated states (Fig. 5H-J and R-T). Furthermore, the free energy maps of all three mutations showed shallower energy wells in the activated states, consistent with their reduced stabilization and their right-shifted voltage-dependence of current activation. Also, compared to wildtype VSD I the three mutants displayed a decreased drop of the energy minima (ΔG) from resting state 3 to the activated state (Fig. 4L and Fig. 5J,T; Fig. 4-figure supplement 2; Supplementary file 1 - Tables 1 and 2). In the two mutations affecting activation kinetics (E87A/E90A and E90A), resting states 2 and 1 collapsed into a single deep energy well (Fig. 4J and 5R), consistent with the notion that in wildtype VSD I sequential formation of ion-pair interactions between E90 and R1, R2, and R3 is required to stabilize the separate resting states of VSD I, and that the transitions between these states slow down activation kinetics (Videos 1-4; Supplementary file 1 - Table 3). Thus, the structures derived from our simulations provide mechanistic explanations for how Ca_v channels determine their unique gating properties.

Notably, the differences of the transition kinetics observed in the MSM analysis between VSD I and VSD IV, and between WT VSD I and the E87A and E90A were manifested in the activating and deactivating direction (Figs. 2, 4, and 5). However, patch clamp analysis of deactivation kinetics in WT

and mutant VSD I did not reflect these differences (Fig. 5-figure supplement 1). Upon repolarization to negative membrane potentials the deactivation time constants of all tested constructs were between 4 to 10 ms and thus near the activation time constants of the fast activating mutants (E87A/E90A and E90A). This is expected considering the distinct dependence of channel activation and deactivation on the actions of multiple VSDs. Upon depolarization, the VSDs need to proceed through all resting states into the activated state before the channel gate will open. Inevitably, the speed of this action is limited by the slowest VSD necessary for channel opening (VSD I in the case of Ca_v1.1). In contrast, on deactivation the channel gate closes when the first essential VSD transits from the activated state into resting state 2 (Fig. 5-figure supplement 1). Principally, this can be any one of the four VSDs. Therefore, channel deactivation will be rapid even if VSD I requires considerably more time to return to its deepest resting state, as predicted by our MSM analysis.

Discussion

Our advanced structure models of the activated and resting states of Ca_v1.1 VSDs fill an important gap in the understanding of the voltage-sensing mechanism in eukaryotic voltage-gated cation channels. The results presented in this study demonstrate two surprisingly different VSDs, which substantially differ in the range of S4 helix displacement during activation/deactivation, as well as in the number and position of ionic bonds formed between the outer gating charges and counter charges of the ENC in the resting and activated states. These structural differences correspond to differences in the free energy states and kinetics of the state transitions, which in turn correlate with the experimentally determined kinetics and voltage-dependences of current activation. Throughout this structure-function study the combination of MD simulation and MSM proved to be of exceptionally high predictive value. All tested interaction partners suggested by the model showed the predicted effects on channel gating when experimentally tested by mutagenesis and electrophysiology analysis. Conversely, alterations of kinetic properties first recognized experimentally were reliably reproduced and explained by our computer model.

Overall, the structures of the lowest energy states of Ca_v1.1 VSDs display the basic features of the sliding helix model (Catterall et al., 2017) and of previous simulations of VSD structures (Tuluc et al., 2016b; Yarov-Yarovoy et al., 2012). Notably, two of the resting states predicted by our models closely correspond to recently described cryo-EM structures of homotetrameric Na_v channels with the VSD in a down-state. Our resting state 1 structure of VSD IVa resembles a mutated Na_vAb captured in the resting state by disulfide locking (C α RMSD of 1.7 Å) (Fig. 2-figure supplement 4) (Wisedchaisri et al., 2019). Our resting state 2 structure of VSD I resembles that of a Na_vAb/Na_v1.7 chimera stabilized in a

deactivated state by toxin binding ($C\alpha$ RMSD of 1.9 Å) (Fig. 2-figure supplement 5) (Xu et al., 2019). Thus, the voltage-sensing action of the eukaryotic $Ca_v1.1$ displays a remarkable similarity to that of its homotetrameric bacterial ancestor. Particularly the sequential movement of the gating charges across the HCS and the stabilization of the states by their transient formation of ion-pairs with negatively charged amino acids of the INC were similarly observed in VSD I and VSD IV. Evidently, these features represent highly conserved properties of voltage-gated cation channels (prokaryotic and eukaryotic) and probably define the essence of the voltage-sensing mechanism.

In contrast, the interactions of the outer gating charges with the negatively charged amino acids of the ENC differed considerably between the two studied VSDs of $Ca_v1.1$, as well as between the two splice variants of VSD IV. Although the outer gating charges of both VSDs established such ion-pairs, they used partners in different transmembrane segments (IS2 vs. IVS3). In both VSDs the examined ion-pair partners of R1 proved to be crucial for stabilizing the voltage sensor in the activated state; as their mutations consistently resulted in a shift of the voltage-dependence of activation to more depolarized voltages (El Ghaleb et al., 2019; Tuluc et al., 2016b). Furthermore, the ion-pair interactions in the two VSDs differed in the extent they were formed in different states. While in VSD IV such ion-pairs were restricted to the activated state, in VSD I they were also found in resting states 2 and 3, leading to a substantially stronger stabilization of these resting states in VSD I compared to VSD IV. Concordantly MSM and site directed mutagenesis demonstrated that this stabilization of resting states in VSD I causes a dramatic slowing of state transitions and of activation kinetics characteristic for $Ca_v1.1$ currents, respectively. Apparently, the repeated formation and breaking of ionic bonds in consecutive resting states increases the energy barriers between the states and thus slows down the movement of IS4 to the activated state. In contrast, the weaker hydrogen bonds of the outer gating charges of IVS4, or mutation of ion-pair partners in IS3 support fast state transitions and current activation.

This indicates that the negative counter charges in the ENC serve a dual role in the voltage-gating process. They enable the hand over hand movement of the gating charges, thus guiding the state-transitions of S4 across the membrane electric field, and they stabilize the VSD in the activated states. Accordingly, mutation of specific counter charges differentially affected the voltage-dependence and kinetics of activation. While the charge-neutralizing mutation of E87 in IS2, which stabilizes the VSD I in the activated state, perturbed the voltage-dependence of activation, mutating E90, which also forms ionic bonds with R1 and R2 in the resting states, accelerated the activation kinetics. MD simulation and MSM suggested that the loss of the stabilizing interactions with the negative countercharge E90 causes the collapse of resting states 1 and 2, thereby enhancing the speed of VSD I transition into the activated state. As E90 also contributed to stabilizing the activated

state, its mutation also caused a right-shift of the voltage-dependence of activation. The importance of activated state-stabilizing interactions of the outermost gating charges for specifically setting the voltage-dependence of activation is consistent with earlier mutagenesis experiments of R1 in VSD I and of R1, R2, and D1196 in VSD IV, all of which right-shifted voltage-dependence without changing activation kinetics (El Ghaleb et al., 2019; Tuluc et al., 2016b). Unlike VSD I, VSD IV establishes stabilizing ion-pairs exclusively in the activated state. The lack of stabilizing ion-pairs in the resting states is consistent with the intrinsically fast activation kinetics of this VSD. However as in VSD I, weakening the counter charges in IVS3 either physiologically, by insertion of exon 29 in the IVS3-S4 linker, or experimentally, by mutagenesis, caused a right-shift of the voltage-dependence of activation with little effect on kinetics (Tuluc et al., 2016b). Thus, ion-pair formation of R1 with E87 and E90 in VSD I, and of R1 in VSD IV with D1196 are functionally equivalent in stabilizing the activated state in both VSDs, whereas ion-pair formation of multiple gating charges with E90 that stabilize the resting states is specific for VSD I and represents the structural correlate of Ca_v1.1 slow activation.

If the outward motion of the S4 helix with the sequential stabilization of the inner gating charges by ion-pair formation with the INC is the general theme of the voltage-sensing process, the interactions between the outer gating charges with counter charges of the ENC represent the variations to this theme. They differ in number, strength and position from analogous interactions described in the structures of other channels, and even between the VSDs of a single channel. Importantly, in which states they are established determines which biophysical properties of channel gating are being modulated. The general principle derived from our modeling and mutagenesis experiments is that stabilization of VSDs in the activated state supports channel opening by shifting the voltage-dependence of activation to more hyperpolarizing potentials. On the other hand, ion-bond formation between the gating charges and the ENC in resting states delays channel opening by slowing down the activation kinetics. Interestingly, at least in Ca_v1.1, these actions are divided between separate VSDs. Thus, our findings provide a molecular mechanism explaining how channels using the same general voltage-sensing mechanism can produce very distinct gating properties and how in pseudo-tetrameric eukaryotic voltage-gated cation channels the distinct VSDs cooperate in establishing the characteristic gating properties.

415 **Materials and Methods**

Key Resources Table				
Reagent type (species) or resource	Designation	Source or reference	Identifiers	Additional information
gene (human)	<i>CACNA1S</i>	Wu et al., Nature, 2016	Q13698	
gene (rabbit)	<i>CACNA1S</i>	Grabner et al., PNAS, 1998	P07293	
cell line (mouse)	GLT, dysgenic skeletal myotubes	Powell et al., JCB 1996	GLT; mdg/mdg	Cav1.1-null
transfected construct (rabbit)	GFP-CaV1.1e (wild type)	Tuluc et al., Biophys J. 2009		Cav1.1-D exon 29
transfected construct (rabbit)	GFP-CaV1.1e -E87A/E90A, -E87A, -E90A	This paper		
antibody	rabbit polyclonal anti-GFP	Invitrogen Thermo Fisher	A-6455, RRID:AB_221570	IF (1:10,000)
antibody	mouse monoclonal anti-RyR	Invitrogen Thermo Fisher	(MA3-925) 34-C RRID: AB_2254138	IF (1:500)
software, algorithm	AMBER Simulation Software	AmberMD	RRID: SCR_014230	
software, algorithm	Ambertools 19	AmberMD	RRID: SCR_018497	
software, algorithm	Pymol	Schrödinger	RRID: SCR_000305	
software, algorithm	Clampex	Clampex	Version 10.2 RRID:SCR_011323	
software, algorithm	Clampfit	Clampfit	Version 10.7 RRID:SCR_011323	
software, algorithm	SigmaPlot	SigmaPlot	Version 12.0 RRID:SCR_003210	
software, algorithm	GraphPad Prism	GraphPad Prism	Version 7 RRID:SCR_002798	

Homology model of the Ca_v1.1 α 1-subunit

We predicted the structure of the human wildtype Ca_v1.1 α 1-subunit by making a homology model based on the cryo-EM structure of the rabbit Cav1.1 α 1-subunit in the inactive state (Wu et al., 2016). Homology modelling has been performed using Rosetta and MOE (Molecular Operating Environment, version 2018.08, Molecular Computing Group Inc., Montreal, Canada). The sequence identity between the rabbit and the human Ca_v1.1 α 1 subunit is 92.6 %, the sequence similarity even 95.6 %. Because of the high sequence similarity and identity between the human and the rabbit Ca_v1.1, we generated only 10 homology models and chose the one model with the best energy score as starting structure for further minimizations, equilibrations and simulations. The fragment-based cyclic coordinate descent (CCD) algorithm implemented in Rosetta was used to generate structures for loops that were not resolved in the Cav1.1 α 1-subunit template (Supplementary file 1 – Table 4; Input scripts - IS1) (Canutescu and Dunbrack, 2003; Wang et al., 2007). The C-terminal and N-terminal parts of each domain were capped with acetylamide (ACE) and N-methylamide to avoid perturbations by free charged functional groups. The structure model was embedded in a plasma membrane consisting of POPC (1-palmitoyl2-oleoyl-sn-glycero-3-phosphocholine) and cholesterol in a 3:1 ratio, using the CHARMM-GUI Membrane Builder (Jo et al., 2009). Water molecules and 0.15 M NaCl were included in the simulation box. Energy minimizations of the wildtype and the mutants in the membrane environment were performed. The topology was generated with the tleap tool of the AmberTools18 (Case et al., 2018), using force fields for proteins and lipids, ff14SBonlysc and Lipid14 (Dickson et al., 2014), respectively. The wildtype and mutant structures were heated from 0 to 300 K in two steps, keeping the lipids fixed, and then equilibrated over 1 ns. Then MD simulations were performed for 10 ns, with time steps of 2 fs, at 300 K and in anisotropic pressure scaling conditions that is suitable for membrane proteins. Van der Waals and short-range electrostatic interactions were cut off at 10 Å, whereas long-range electrostatics were calculated by the Particle Mesh Ewald (PME) method. A hierarchical clustering was performed on the 10 ns trajectory using a RMSD distance cut-off criterion of 2.5 Å, resulting in three clusters. We chose the highest populated cluster representative for all further steps. Pymol Molecular Graphics System was used to visualize the key interactions and point out differences in the wildtype and mutant structures (The PyMOL Molecular Graphics System, Version 2.0 Schrödinger, LLC.).

Enhanced sampling and molecular dynamics simulation protocol

Because high-resolution structures of resting states of Ca_v and Na_v channels are still lacking, we applied molecular dynamics (MD) simulation and Markov-state modeling (MSM) of individual VSD in the context of the whole channel to predict the structures and energy levels of resting states (Chodera and Noé, 2014). The work-flow of the modeling procedure is summarized in Fig. 2-figure supplement 1. To overcome the high energy barriers and the timescale limitations of MD simulations,

we applied Umbrella sampling as enhanced sampling technique. As collective variable we used the distances between the S4 gating charge residues (R1, R2 and R3) and anchor residues at the intracellular helical ends of the voltage-sensing domains located in S1 and S3, by using a force constant of the harmonic spring potential of $80 \text{ kcal/mol} \cdot \text{\AA}^2$ to pull the S4 helix downwards. Starting from the equilibrated structure, the Umbrella windows decreased between a distance of 24.0 to 14.0 Å using a step-size of 1 Å. Each Umbrella window was simulated for 100 ns. After 20 ns of simulation time, the current conformation was extracted and used as starting structures for the next Umbrella window. The force constant of $80 \text{ kcal/mol} \cdot \text{\AA}^2$ was determined to allow a sliding movement of S4 with minimal distortion of the VSDs. Additionally, we applied a weak backbone restraint on the ϕ torsion angle of the S4 helix of $50 \text{ kcal/mol} \cdot \text{rad}^2$ to guarantee a minimum of local artifacts of the Umbrella sampling process, i.e., loss of secondary structure of the S4 helix. This combination of pulling and torsional restraint was tested and resulted in a sliding movement of the S4 helix without observing unfolding events. Note that the combination of restraints and Umbrella sampling does not result in equilibrium distributions, due to insufficient overlap between the individual sampling windows. Rather the Umbrella sampling was applied to generate conformations along a potential deactivation pathway; however, no states were pre-defined based on the Umbrella sampling. Hence, the Umbrella sampling was used as a mechanical force to pull the S4 helix in the absence of a membrane potential. To obtain the different activation and resting states, we used the resulting pathway of the combined Umbrella sampling trajectories and clustered it using a small distance cut-off criterion to also obtain cluster representatives at transition state regions. Using this procedure, we cannot exclude the possibility of other substantially different pathways (e.g. such that involve helix rotation and formation or breaking of interactions before or after S4 translocation). However, from our calculations we see no indications of the existence of such completely different pathways, which are kinetically accessible. Thus, to reconstruct the transition kinetics and to improve the sampling efficiency, we clustered the Umbrella sampling trajectories applying the program implemented in the AMBER suite *cpptraj* (Roe and Cheatham, 2013) by using the average linkage hierarchical clustering algorithm with a RMSD distance cut-off criterion of 1.2 Å resulting in a large number of clusters. The choice of the distance cut-off is optimized to obtain a broad cluster distribution within the conformational space of each VSD. The cluster representatives of the different activation states were equilibrated and simulated for 100 ns using the AMBER18 simulation package. For the resulting trajectories a time-lagged independent component analysis (tICA) was performed using the python library PyEMMA 2 employing a lag time of 10 ns.

Construction of tICA and Markov state models

tICA is a dimensionality reduction technique, detecting the slowest-relaxing degrees of freedom and facilitating the kinetic clustering, which is crucial for building an MSM (Pérez-Hernández and Noé,

2016). It linearly transforms a set of high-dimensional input coordinates to a set of output coordinates, by finding a subspace of good reaction coordinates. Thereby, tICA finds coordinates of maximal autocorrelation at a given lag time. The lag time sets a lower limit to the timescales considered in the tICA and the MSM.

Thermodynamics and kinetics were calculated with a Markov-state model by using PyEMMA 2 (Scherer et al., 2015), which uses the k-means clustering algorithm to define microstates and the PCCA+ clustering algorithm to coarse grain the microstates to macrostates (Röblitz and Weber, 2013; Wu and Noé, 2020). The k-means clustering represents an iterative and robust clustering algorithm, which partitions the dataset into pre-defined distinct non-overlapping clusters, with the aim to make the intra-cluster points as similar as possible and keeping the subgroups as different as possible.

To construct coarse-grained models the Perron Cluster Cluster Analysis (PCCA) uses the eigenspectrum of a transition probability matrix. The eigenvectors corresponding to the Perron Cluster can be further used to coarse-grain a MSM. Here, we applied the PCCA+ clustering, as it is more robust than PCCA. PCCA+ tries to identify a set of indicator functions that can reproduce the slowest dynamical eigenvectors. PCCA+ relies on a maximum likelihood estimate of the transition.

To build the Markov-state model we used the $C\alpha$ coordinates of the respective S4 transmembrane helix, defined 100 microstates using the k-means clustering algorithm and applied a lag time of 10 ns. The sampling efficiency and the reliability of the Markov-state model (e.g., defining optimal feature mappings) can be evaluated with the Chapman-Kolmogorov test (Fig.S4), by using the variational approach for Markov processes and by taking into account the fraction of states used, as the network states must be fully connected to calculate probabilities of transitions and the relative equilibrium probabilities (Likas et al., 2003). The construction of the MSM allows to quantify thermodynamic and kinetic properties of the resulting ensembles without the intrinsic bias resulting from the seeding process (Fig. 2-figure supplement 1). The first stage of the MSM is to discretize the obtained conformational space into so-called microstates, grouping together conformations of the system that can exchange rapidly (e.g., by k-means clustering). The aim is to construct a kinetically relevant clustering by using a geometric criterion, which still allows a quantitative connection with experiments, due to their high resolution. To identify the kinetic relevance of the clustering, an appropriate lag time, i.e., observation interval, has to be chosen. This resulting microstate model can then be used as starting point for a kinetic clustering. To create a more understandable model, a kinetic clustering of a relevant set of microstates to so-called macrostates, can be performed, which are larger aggregates that correspond to the free energy wells (e.g., by PCCA+ clustering). The additional kinetic clustering into macrostates results in a more compact representation than the microstate model and thereby allows an easier processing and understanding of the conformational

space. Thus, these qualitative models are ideal for generating new hypotheses, which can then be tested again with higher resolution models and experiments. The MSM was constructed by following the guidelines and input commands from the provided tutorial (<http://www.emma-project.org/latest/tutorial.html#jupyter-notebook-tutorials>).

To calculate the 1D free energy barriers K^\ddagger we used the obtained mean first passage times k from the MSM and calculated the barriers according to the transition state theory with the equation below.

$$k = \frac{k_B T}{h} * K^\ddagger$$

Expression plasmids

Cloning procedure for GFP-Ca_v1.1e WT was previously described (Tuluc et al., 2009). For better comparison with the literature the non-corrected version of Ca_v1.1 was used. This Ca_v1.1 construct contains a lysine in position R1 of the VSD I, that results in a 12 mV left-shifted V_{1/2} compared to the construct with the evolutionary conserved arginine in position R1 (El Ghaleb et al., 2019). To generate the double mutant GFP-Ca_v1.1e-E87A/E90A and the single mutants GFP-Ca_v1.1e-E87A and GFP-Ca_v1.1e-E90A, aa E87 and E90 were neutralized by SOE-PCR (Table S5). Briefly, nt 1–1113 of the coding sequence of Ca_v1.1e (nt 226-1338 of *CACNA1S* NCBI reference sequence NM_001101720.1) were PCR amplified with overlapping primers introducing the point mutation A > C at position nt 260 and/or the point mutation A > G at position nt 269 (nt 485 and nt 494, respectively, of NM_001101720.1) in separate PCR reactions using GFP-Ca_v1.1e-WT as template. The two separate PCR products were then used as templates for a final PCR reaction with flanking primers to connect the nucleotide sequences. This fragment was then Sall/EcoRI digested and cloned into the respective sites of GFP-Ca_v1.1e WT. Sequence integrity of the newly generated constructs was confirmed by sequencing (MWG Biotech, Martinsried, Germany).

Cell culture and transfection

Myoblasts of the dysgenic (mdg/mdg) cell line GLT were cultured as previously described in Powell et al. (Powell et al., 1996). Briefly, cells were plated on 35 mm culture dishes and transfected with 0.5 µg of the desired Ca_v1 subunit 4 days after plating using FuGENE-HD transfection reagent (Promega). After 7 to 8 days in culture, transfected myotubes showing GFP fluorescence were analyzed by electrophysiology or fixed for immunolabeling after 9 to 10 days in culture. The auxiliary calcium channel subunits α2δ-1, β1a, and γ₁, along with the STAC3 protein and ryanodine receptor, are endogenously expressed by GLT myotubes, enabling functional membrane incorporation of the channel constructs in the triad junction.

Immunofluorescence and antibodies

Paraformaldehyde-fixed cultures were immunolabeled as previously described (Flucher et al., 1994) with rabbit polyclonal anti-GFP (1:10,000; Invitrogen Thermo Fisher) and mouse monoclonal anti-RyR (34-C; 1:500; Invitrogen Thermo Fisher) and fluorescently labeled with goat anti-rabbit Alexa-488 and secondary goat anti-mouse Alexa-594 (1:4000), respectively. Thus, the anti-GFP label and the intrinsic GFP signal were both recorded in the green channel. Samples were observed using a 60X, 1.42 NA objective with a BX53 Olympus microscope and 14-bit images were captured with a cooled charge-coupled device camera (XM10, Olympus) and CellSens Dimension image-processing software (Olympus). Image composites were arranged in Adobe Photoshop CS6 (Adobe Systems INC.) and linear adjustments were performed to correct black level and contrast.

Electrophysiology and data analysis

Calcium currents were recorded with the whole-cell patch-clamp technique in voltage-clamp mode using an Axopatch 200A amplifier (Axon Instruments). Patch pipettes (borosilicate glass; Science Products) had resistances between 1.5 and 3.5 MΩ when filled with (mM) 145 Cs-aspartate, 2 MgCl₂, 10 HEPES, 0.1 Cs-EGTA, and 2 Mg-ATP (pH 7.4 with CsOH). The extracellular bath solution contained (mM) 10 CaCl₂, 145 tetraethylammonium chloride, and 10 HEPES (pH 7.4 with tetra-ethylammonium hydroxide). Data acquisition and command potentials were controlled by pCLAMP software (Clampex version 10.2; Axon Instruments); analysis was performed using Clampfit 10.7 (Axon Instruments) and SigmaPlot 12.0 (SPSS Science) software. The current-voltage dependence was fitted according to

$$I = G_{\max} * (V - V_{\text{rev}}) / (1 + \exp(-(V - V_{1/2})/k))$$

where G_{\max} is the maximum conductance of the L-type calcium currents, V_{rev} is the extrapolated reversal potential of the calcium current, $V_{1/2}$ is the potential for half maximal conductance, and k is the slope. The conductance was calculated using $G = (-I * 1000) / (V_{\text{rev}} - V)$, and its voltage dependence was fitted according to a Boltzmann distribution:

$$G = G_{\max} / (1 + \exp(-(V - V_{1/2})/k))$$

Statistical analysis

All four experimental groups were analyzed in transiently transfected cells from 3 to 5 independent cell passages. The E87A/E90A, E87A and E90A variants of Cav1.1e were always recorded in parallel with the WT Cav1.1e in cells of the same passage to obtain the best controls for statistical

comparison. Consequently, the values for wildtype controls vary slightly between conditions. The means, standard errors (SE), and p-values were calculated using the student *t*-test, 2-tailed, with significance criteria $p < 0.05$ *, $p < 0.01$ **, and $p < 0.001$ ***). Two-way repeated measure ANOVA, with the Holm Sidak posthoc test, was used to calculate p-values of deactivation.

Data and Materials Availability.

All relevant data are included in the manuscript or Supplementary Information. The Rosetta models for VSD I and VSD IV, as well as the pdb structures of the models of the activated and resting states of both the WT and the mutant VSDs are available from the Dryad server <https://doi.org/10.5061/dryad.hhmgqnkfd>. Expression plasmids are available with materials transfer agreement from B.E.F., Medical University Innsbruck.

ACKNOWLEDGMENTS

We thank I. Mahlknecht, N. Kranebitter, M. Bacher and S. Demetz for excellent technical support. The computational data have been obtained in part using the Vienna Scientific Cluster (VSC).

Funding: The work was supported by funds from the Austrian Science Fund (FWF) P30402 and DOC30 (to B.E.F.), T855 (to M.C).

Declaration of interests: The authors declare no competing interests.

References

- Ahern CA, Payandeh J, Bosmans F, Chanda B. 2016. The hitchhiker's guide to the voltage-gated sodium channel galaxy. *J Gen Physiol* **147**:1–24. doi:10.1085/jgp.201511492
- Bender BJ, Cisneros A, Duran AM, Finn JA, Fu D, Lokits AD, Mueller BK, Sangha AK, Sauer MF, Sevy AM, Sliwoski G, Sheehan JH, DiMaio F, Meiler J, Moretti R. 2016. Protocols for molecular modeling with Rosetta3 and RosettaScripts. *Biochemistry* **55**:4748–4763. doi:10.1021/acs.biochem.6b00444
- Canutescu AA, Dunbrack RL. 2003. Cyclic coordinate descent: A robotics algorithm for protein loop closure. *Protein Sci* **12**:963–972. doi:10.1110/ps.0242703
- Case DA, Ben-Shalom IY, Brozell SR, Cerutti DS, Cheatham TEI, Cruzeiro VWD, Darden TA, Duke RE, Ghoreishi D, Gilson MK, Gohlke H, Goetz AW, Greene D, Harris R, Homeyer N, Izadi S, Kovalenko A, Kurtzman T, Lee TS, LeGra S, York DM, Kollman PA. 2018. AMBER 2018. *Univ California, San Fr.*
- Catterall WA, Lenaus MJ, El-Din TMG. 2020. Structure and pharmacology of voltage-gated sodium and calcium channels. *Annu Rev Pharmacol Toxicol* **60**:1–22. doi:10.1146/annurev-pharmtox-010818-021757
- Catterall WA, Wisedchaisri G, Zheng N. 2017. The chemical basis for electrical signaling. *Nat Chem Biol* **13**:455–463. doi:10.1038/nchembio.2353
- Chodera JD, Noé F. 2014. Markov state models of biomolecular conformational dynamics. *Curr Opin Struct Biol* **25**:135–44. doi:10.1016/j.sbi.2014.04.002
- Dickson CJ, Madej BD, Skjevik AA, Betz RM, Teigen K, Gould IR, Walker RC. 2014. Lipid14: The Amber lipid force field. *J Chem Theory Comput* **10**:865–879. doi:10.1021/ct4010307
- El Ghaleb Y, Campiglio M, Flucher BE. 2019. Correcting the R165K substitution in the first voltage-

- 626 sensor of CaV1.1 right-shifts the voltage-dependence of skeletal muscle calcium channel
627 activation. *Channels (Austin)* **13**:62–71. doi:10.1080/19336950.2019.1568825
- 628 Flucher BE. 2020. Skeletal muscle Ca V 1 . 1 channelopathies 739–754.
- 629 Flucher BE. 2016. Specific contributions of the four voltage-sensing domains in L-type calcium
630 channels to gating and modulation. *J Gen Physiol* **148**:91–95. doi:10.1085/jgp.201611663
- 631 Flucher BE, Andrews SB, Daniels MP. 1994. Molecular organization of transverse tubule/sarcoplasmic
632 reticulum junctions during development of excitation-contraction coupling in skeletal muscle.
633 *Mol Biol Cell* **5**:1105–1118. doi:10.1091/mbc.5.10.1105
- 634 Jensen M, Jogini V, Borhani DW, Leffler AE, Dror RO, Shaw DE. 2012. Mechanism of voltage gating in
635 potassium channels. *Science (80-)* **336**:229–233. doi:10.1126/science.1216533
- 636 Jo S, Lim JB, Klauda JB, Im W. 2009. CHARMM-GUI membrane builder for mixed bilayers and its
637 application to yeast membranes. *Biophys J* **97**:50–58. doi:10.1016/j.bpj.2009.04.013
- 638 Laidler KJ, King MC. 1983. The development of transition-state theory. *J Phys Chem* **87**:2657–2664.
639 doi:10.1021/j100238a002
- 640 Lenaeus MJ, Gamal El-Din TM, Ing C, Ramanadane K, Pomès R, Zheng N, Catterall WA. 2017.
641 Structures of closed and open states of a voltage-gated sodium channel. *Proc Natl Acad Sci*
642 **114**:E3051–E3060. doi:10.1073/pnas.1700761114
- 643 Likas A, Vlassis N, J. Verbeek J. 2003. The global k-means clustering algorithm. *Pattern Recognit*
644 **36**:451–461. doi:10.1016/S0031-3203(02)00060-2
- 645 Nakai J, Adams BA, Imoto K, Beam KG. 1994. Critical roles of the S3 segment and S3-S4 linker of
646 repeat I in activation of L-type calcium channels. *Proc Natl Acad Sci* **91**:1014–1018.
- 647 Pan X, Li Z, Zhou Q, Shen H, Wu K, Huang X, Chen J, Zhang J, Zhu X, Lei J, Xiong W, Gong H, Xiao B, Yan
648 N. 2018. Structure of the human voltage-gated sodium channel Nav1.4 in complex with β 1.
649 *Science (80-)* **362**. doi:10.1126/science.aau2486
- 650 Pantazis A, Savalli N, Sigg D, Neely A, Olcese R. 2014. Functional heterogeneity of the four voltage
651 sensors of a human L-type calcium channel. *Proc Natl Acad Sci* **111**:18381–18386.
652 doi:10.1073/pnas.1411127112
- 653 Payandeh J, Scheuer T, Zheng N, Catterall WA. 2011. The crystal structure of a voltage-gated sodium
654 channel. *Nature* **475**:353–358. doi:10.1038/nature10238
- 655 Pérez-Hernández G, Noé F. 2016. Hierarchical time-lagged independent component analysis:
656 Computing slow modes and reaction coordinates for large molecular systems. *J Chem Theory*

- 657 *Comput* **12**:6118–6129. doi:10.1021/acs.jctc.6b00738
- 658 Powell JA, Petherbridge L, Flucher BE. 1996. Formation of triads without the dihydropyridine
659 receptor subunits in cell lines from dysgenic skeletal muscle. *J Cell Biol* **134**:375–387.
660 doi:10.1083/jcb.134.2.375
- 661 Röblitz S, Weber M. 2013. Fuzzy spectral clustering by PCCA+: application to Markov state models
662 and data classification. *Adv Data Anal Classif* **7**:147–179. doi:10.1007/s11634-013-0134-6
- 663 Roe DR, Cheatham TE. 2013. PTRAJ and CPPTRAJ: Software for processing and analysis of molecular
664 dynamics trajectory data. *J Chem Theory Comput* **9**:3084–95. doi:10.1021/ct400341p
- 665 Rohl CA, Strauss CEM, Misura KMS, Baker D. 2004. Protein structure prediction using Rosetta.
666 *Methods Enzymol* **383**:66–93. doi:10.1016/S0076-6879(04)83004-0
- 667 Scherer MK, Trendelkamp-Schroer B, Paul F, Pérez-Hernández G, Hoffmann M, Plattner N, Wehmeyer
668 C, Prinz J-H, Noé F. 2015. PyEMMA 2: A software package for estimation, validation, and
669 analysis of Markov models. *J Chem Theory Comput* **11**:5525–42. doi:10.1021/acs.jctc.5b00743
- 670 Tanabe T, Beam KG, Powell JA, Numa S. 1988. Restoration of excitation-contraction coupling and
671 slow calcium current in dysgenic muscle by dihydropyridine receptor complementary DNA.
672 *Nature* **336**:134–9. doi:10.1038/336134a0
- 673 Tao X, Lee A, Limapichat W, Dougherty DA, MacKinnon R. 2010. A gating charge transfer center in
674 voltage sensors. *Science (80-)* **328**:67–73. doi:10.1126/science.1185954
- 675 Tuluc P, Benedetti B, Coste De Bagneaux P, Grabner M, Flucher BE. 2016a. Two distinct voltage-
676 sensing domains control voltage sensitivity and kinetics of current activation in CaV1.1 calcium
677 channels. *J Gen Physiol* **147**:437–449. doi:10.1085/jgp.201611568
- 678 Tuluc P, Molenda N, Schlick B, Obermair GJ, Flucher BE, Jurkat-Rott K. 2009. A Cav1.1 Ca²⁺ channel
679 splice variant with high conductance and voltage-sensitivity alters EC coupling in developing
680 skeletal muscle. *Biophys J* **96**:35–44. doi:10.1016/j.bpj.2008.09.027
- 681 Tuluc P, Yarov-Yarovoy V, Benedetti B, Flucher BE. 2016b. Molecular interactions in the voltage
682 sensor controlling gating properties of CaV calcium channels. *Structure* **24**:261–271.
683 doi:10.1016/j.str.2015.11.011
- 684 Wang C, Bradley P, Baker D. 2007. Protein-protein docking with backbone flexibility. *J Mol Biol*
685 **373**:503–519. doi:10.1016/j.jmb.2007.07.050
- 686 Wisedchaisri G, Tonggu L, Gamal El-Din TM, McCord E, Zheng N, Catterall WA. 2021. Structural basis
687 for high-affinity trapping of the NaV1.7 channel in its resting state by tarantula toxin. *Mol Cell*
688 **81**:38-48.e4. doi:10.1016/j.molcel.2020.10.039

- 689 Wisedchaisri G, Tonggu L, McCord E, Gamal El-Din TM, Wang L, Zheng N, Catterall WA. 2019. Resting-
690 state structure and gating mechanism of a voltage-gated sodium channel. *Cell* **178**:993-
691 1003.e12. doi:10.1016/j.cell.2019.06.031
- 692 Wu H, Noé F. 2020. Variational approach for learning Markov processes from time series data. *J*
693 *Nonlinear Sci* **30**:23–66. doi:10.1007/s00332-019-09567-y
- 694 Wu J, Yan Z, Li Z, Qian X, Lu S, Dong M, Zhou Q, Yan N. 2016. Structure of the voltage-gated calcium
695 channel Cav1.1 at 3.6 Å resolution. *Nature* **537**:191–196. doi:10.1038/nature19321
- 696 Wu J, Yan Z, Li Z, Yan C, Lu S, Dong M, Yan N. 2015. Structure of the voltage-gated calcium channel
697 Cav1.1 complex. *Science (80-)* **350**:aad2395-1–9. doi:10.1126/science.aad2395
- 698 Xu H, Li T, Rohou A, Arthur CP, Tzakoniati F, Wong E, Estevez A, Kugel C, Franke Y, Chen J, Ciferri C,
699 Hackos DH, Koth CM, Payandeh J. 2019. Structural basis of Nav1.7 inhibition by a gating-
700 modifier spider toxin. *Cell* **176**:702–715. doi:10.1016/j.cell.2018.12.018
- 701 Yan Z, Zhou Q, Wang L, Wu J, Zhao Y, Huang G, Peng W, Shen H, Lei J, Yan N. 2017. Structure of the
702 Nav1.4-β1 Complex from Electric Eel. *Cell* **170**:470-475.e11. doi:10.1016/j.cell.2017.06.039
- 703 Yarov-Yarovoy V, DeCaen PG, Westenbroek RE, Pan C-Y, Scheuer T, Baker D, Catterall WA. 2012.
704 Structural basis for gating charge movement in the voltage sensor of a sodium channel. *Proc*
705 *Natl Acad Sci U S A* **109**:E93-102. doi:10.1073/pnas.1118434109
- 706 Zhang X, Ren W, DeCaen P, Yan C, Tao X, Tang L, Hasegawa K, Kumasaka T, He J, Wang JJ, Clapham
707 DE, Yan N, Hasegawa K, Kumasaka T, He J, Wang JJ, Clapham DE, Yan N. 2012. Crystal structure
708 of an orthologue of the NaChBac voltage-gated sodium channel. *Nature* **486**:130–134.
709 doi:10.1038/nature11054
- 710 Zhao Y, Huang G, Wu J, Wu Q, Gao S, Yan Z, Lei J, Yan N. 2019. Molecular basis for ligand modulation
711 of a mammalian voltage-gated Ca²⁺ channel. *Cell* **177**:1495–1506.
712 doi:10.1016/j.cell.2019.04.043
- 713

Figure Legends

Figure 1: Structure model of the hetero-tetrameric human $\text{Ca}_v1.1$. (A) Domain structure of eukaryotic Ca_v channels. (B) Structure model of the human $\text{Ca}_v1.1$ α_1 subunit (top view; color-code as in A) refined with MD simulation in a membrane environment (see Materials and Methods) based on the 3.6Å structure of rabbit $\text{Ca}_v1.1$ (Pan et al., 2018; Wu et al., 2016). (C) Sequence alignment of the S4 helices of each $\text{Ca}_v1.1$ VSD compared to the homo-tetrameric Na_vAb ; gating charges (R, K) are indicated in blue. (D) Structure of a single repeat (IV) within the space-filling model of $\text{Ca}_v1.1$. (E) Structural overlay of Na_vAb with VSD IV of $\text{Ca}_v1.1$. (F) Cylindrical representation of the VSD structure showing the positive gating charges in S4 (blue) and counter charges (red) of the inner and extracellular negative clusters (INC, ENC) in S1, S2, and S3. The phenylalanine in S2, marking the hydrophobic constriction site (HCS), is indicated in green. Ribbon models of the four VSDs of $\text{Ca}_v1.1$ in the up-state, showing the side chains of the S4 gating charges (R, light blue; K, dark blue) and their putative ion-pair partners (red). Note that the numbers and positions of the ion-pair interactions in the ENC differ between the VSDs.

Figure 1-figure supplement 1: Structure comparison of the four VSD of $\text{Ca}_v1.1$ with the VSD of Na_vAb . Comparison of the individual four VSD of $\text{Ca}_v1.1$ with the VSD of Na_vAb (Payandeh et al., 2011) illustrates the overall similarity with the ancestral channel. At the same time highlights the structural differences between the $\text{Ca}_v1.1$ VSDs. Na_vAb , orange; $\text{Ca}_v1.1$ VSD are color-coded according to Figure 1A; exon 29 in the S3-S4 linker of VSD IVa is shown in yellow.

Figure 1-figure supplement 2: Structure comparison between the four VSD of $\text{Ca}_v1.1$. Structural overlay of all four VSD with each other to visualize the structural differences between each VSD. The first mentioned of each pair is shown in turquoise, the second in gray; exon 29 in the IVS3-S4 loop is shown in yellow. The RMSD values calculated of the VSDs without loops indicate the similarities of VSD I with VSD III, and of VSD II with VSD IV. Insertion of exon 29 in VSD IVa decreases its structural similarity with the other VSDs.

Figure 2: MD simulation and kinetics of voltage sensor transitions of VSD I and VSD IV with and without exon 29. (A,E,I) The free energy surfaces of 5.0 μs trajectories of VSD I (A), VSD IV of $\text{Ca}_v1.1\text{e}$ (E), and $\text{Ca}_v1.1\text{a}$ including exon 29 (I) reconstructed in the tICA coordinate space resulted in four macrostates. (B,F,J) Representative structures of each VSD in the four macrostates correspond to three resting and the activated states. The S4 gating charges (blue) show a sequential movement relative to the phenylalanine (green) in the HCS and stabilizing interactions with ion-pair partners (red) and h-bond donors/acceptors (pink) in the INC and ENC. Transition kinetics (in μs) were

calculated using a Markov state model. **(C,G,K)** Overlays of the activated (magenta) and resting state 1 (cyan) illustrating the maximum displacement of S4 during activation. **(D,H,L)** Schematic 1D representations of the free energy surface of VSD I **(D)**, VSD IV of Ca_v1.1e **(H)** and Ca_v1.1a **(L)**, with energy barriers calculated using transition state theory at 0 mV favoring the activated state. Gray trace in **(H)** shows free energy surface of **(D)** for comparison; gray trace in **(L)** shows free energy surface of **(H)** for comparison. Because in skeletal muscle cells VSDs II and III probably control excitation-contraction coupling (Flucher, 2020, 2016) and their contribution to channel gating is less well understood, we did not include them in the present study.

Figure 2-figure supplement 1: Schematic illustration of our robust protocol for describing and characterizing protein dynamics and statistically validating the results by constructing a Markov-state model (MSM).

1) We applied Umbrella sampling as enhanced sampling technique to overcome the timescale limitations of classical molecular dynamics with the aim to generate structurally diverse starting points for further MD simulations along the putative activation pathway.

2) The resulting Umbrella trajectories were clustered geometrically resulting in the distinct starting structures for subsequent classical MD simulations.

3) The obtained trajectories (aggregated simulation time close to 5 μ s) were used to construct a tICA (time-lagged independent component analysis). This kinetic coordinate system represents the basis for the MSM. The symbolic structures in the center show the movements represented by TIC1 and TIC2.

4) To allow subsequent MSM, so-called microstates have to be identified by applying k-means clustering.

5) These microstates are coarse-grained into macrostates by performing spectral clustering.

6) The free energy surface and the transition times are obtained by including the resulting weights and probabilities of the MSM.

Note that the figures represent schematic examples and not data from the present modeling.

Figure 2-figure supplement 2: 3_{10} helix content of the S4 helices of Ca_v1.1 VSDs I and IV in the activated and resting state 1. As predicted by the sliding helix model the S4 helices of Ca_v1.1 VSD I (left) and VSD IV (right) assume a 3_{10} helical conformation, thus aligning consecutive gating charges in one direction. The length and position of this 3_{10} helical stretch differ between the two VSDs and between the activated and resting states.

Figure 2-figure supplement 3: Parameter selection and validation of the MSMs corresponding to the results presented in Figs. 2, 4 and 5. Implied timescales as function of lag time for each system (top). A lag time of 100 steps has been selected to build the MSM. The Chapman-Kolmogorov tests

(bottom) for the respective MSM of each VSD demonstrate the reliability of our MSM. The individual panels of the Chapman-Kolmogorov tests show transitions between two states as labelled respectively. The x-axis denotes multiples of the lag time, the y-axis represents the probability. The plots show a comparison between MSMs estimated at higher lag times and depict extrapolations of the MSMs at a single lag time.

Figure 2-figure supplement 4: Structural comparison of the Ca_v1.1 VSD I resting states with the experimentally determined resting state structure of a Na_v1.7/NaVAb chimera. Comparison of the Cryo-EM structure of VSD II of Na_v1.7/NavAb stabilized in a resting state by toxin binding (PDB accession code 6N4R) (Xu et al., 2019) (green), with the resting states of Ca_v1.1 VSD I obtained by our MD simulation. We observed the highest structural similarity of the VSD II of Na_v1.7/NavAb with our resting state 2 (grey) (C α RMSD of 1.9 Å).

Figure 2-figure supplement 5: Structural comparison of the Ca_v1.1 VSD IV resting states with the experimentally determined resting state structure of Na_vAb. Comparison of the Cryo-EM structure of VSD of Na_vAb stabilized in a resting state by toxin binding (PDB accession code 6P6W) (Wisedchaisri et al., 2019) (cyan), with the resting states of Ca_v1.1 VSD IV obtained by our MD simulation. We observed the highest structural similarity of the Na_vAb VSD with our resting state 1 (grey) (C α RMSD of 1.7 Å).

Figure 3: Ion-pair partners of Ca_v1.1 VSD I and IV gating charges in activated and resting states. (A) Tabular overview of ion-pair interactions of the positive gating charges (blue) with counter charges (red) observed in the activated and three resting states of VSD I, VSD IVa, and VSD IVe. Fields shaded in green show the sequential interaction with the ion-pair partners of the INC. In VSD I this transition through the CTS involves R4, R3, R2, R1, whereas in VSD IV only R4 and R3 participate in equivalent interactions. Ion-pair formation with the ENC (pink shading) of VSD I involved three gating charges (R3, R2, R1) in the activated and intermediate resting states 2 and 3. In VSD IV ion-pair formation with the ENC is limited to the activated state, and it is further reduced by inclusion of exon 29 in VSD IVa. **(B)** Structure overlay of VSD I, VSD IVa (including exon 29; yellow), and VSD IVe in the activated state. **(C)** Schematic representation of the three VSDs indicating similar ion-pair formation in the INC, representing the conserved CTC (dark green), but highly distinct ion-pair formation in the ENC (light green) of the three analyzed VSDs.

Figure 4: Counter charges E87 and/or E90 in IS2 determine the voltage-dependence and kinetics of $\text{Ca}_v1.1$ current activation and VSD transitions. (A) Schematic model of VSD I in the activated and resting states, showing the putative loss of interactions between gating charges and counter charges E87 and E90 upon their mutation to alanine. (B-I) In $\text{Ca}_v1.1\text{e}$ the double mutation E87A/E90A (orange) accelerated activation kinetics and right-shifted the voltage-dependence of activation, compared to wildtype $\text{Ca}_v1.1\text{e}$ (red). (B,C) Representative current traces at V_{max} of WT $\text{Ca}_v1.1\text{e}$ (20 mV) and $\text{Ca}_v1.1\text{e}$ E87A/E90A (40 mV), respectively, and normalized currents at V_{max} (D). (E) Scatter plot of the time to peak; (F) current-voltage relationship; (G) scatterplot of maximum current density ($p=0.03$) (H) voltage-dependence of activation; (I) scatter plot of the voltage at half-maximal activation ($V_{1/2}$). Mean \pm SEM; p-values calculated with student t-test, *** $p<0.00001$. (J,K) The tICA free energy surface of $\text{Ca}_v1.1\text{e}$ E87A/E90A displays three macrostates with structures corresponding to the activated state and resting states 1 and 3, and transition kinetics in the low microsecond timescale. (L) The 1D energy plot shows substantially lower calculated energy barriers between the states of the double mutant (black) compared to the wildtype VSD I (gray).

Figure 4-figure supplement 1: Expression and triad targeting of WT and E87A, E90A mutant GFP- $\text{Ca}_v1.1\text{e}$ channels in dysgenic myotubes. Dysgenic ($\text{Ca}_v1.1$ -null) myotubes were transfected with the indicated GFP- $\text{Ca}_v1.1\text{e}$ constructs and myotubes were fixed and double-immunofluorescence labeled with anti-GFP (to localize the $\text{Ca}_v1.1$ construct) and anti-RyR1 (as a triad marker). Colocalization of GFP- $\text{Ca}_v1.1\text{e}$ constructs with RyR1 in clusters indicates its normal incorporation into triadic calcium channel complexes of skeletal myotubes. All three used GFP- $\text{Ca}_v1.1\text{e}$ mutants (E87A/E90A, E87A and E90A) showed similar expression and distribution as the wildtype GFP- $\text{Ca}_v1.1\text{e}$. Scale bars, 10 μm .

Figure 4-figure supplement 2: Putative counter charge E90, but not E87, determines slow activation kinetics of VSD I. (A-C) scatter plots of the time constant of activation, when fitted to a bi-exponential function (fast and slow component) or to a mono exponential function (mono). (A) This scatter plot shows that, when counter charges E87 and E90 are simultaneously neutralized, kinetics of activation becomes best described by a mono exponential function due to the loss of the slow component; this time constant of E87A/E90A is faster than that of the mono exponential fit of $\text{Ca}_v1.1\text{e}$ WT (WT mono, red; E87A/E90A mono, orange; $p=0.0003$ calculated with the student t-test) and even faster than WT fast (maroon) when $\text{Ca}_v1.1\text{e}$ WT activation is fitted to a bi-exponential function. (B) The scatter plot for E87A shows that, when only this counter charge is neutralized, activation is still best fitted to a bi-exponential function as in $\text{Ca}_v1.1\text{e}$ WT. No significant differences were found between WT slow vs. E87A slow ($p=0.24$, student t-test) and WT fast vs. E87A fast ($p=0.20$, student t-test). When activation is forced to a mono exponential function, no differences were found between WT mono and E87A mono ($p=0.84$, student t-test). (C) When counter charge

E90 alone is neutralized, kinetics of activation is best described by a mono exponential function due to a complete loss of the slow component; the time constant of E90A is faster than the mono exponential fit of Cav1.1e WT (WT mono, red; E90A mono, purple; $p=0.003$) and even faster than WT fast (maroon) when Cav1.1e WT activation is fitted to a bi-exponential function. **(D-F)** bar graphs show the current contribution of the slow vs fast component of activation, when fitted best to a bi-exponential function (Cav1.1e WT in D, E and F and CaV1.1e E87A in E). **(D)** Cav1.1e WT is best fitted to a bi-exponential function with a 31.9:68.1 % ratio of fast:slow. Cav1.1e E87A/E90A can only be described by a mono exponential function, indicating a 100 % contribution of the fast component. **(E)** Activation of both Cav1.1e WT and E87A are best described bi-exponentially, with a somewhat bigger current contribution of the slow component (A_{slow}) in the mutant (A_{slow} WT vs. E87A is 63.8 % vs. 80.8 %, $p=0.052$ calculated with the student t-test). **(F)** E90A can only be described by a mono exponential function, indicating a loss of the slow component. **(G-I)** scatter plots showing the fractional inactivation at the end of the 500 ms test pulse. None of the mutations affected the inactivation properties of Cav1.1 (p -values calculated with the student t-test are 0.31 in G, 0.16 in H and 0.10 in I, see Supplementary file 1 – Table 2).

Figure 5: Counter charges E87 and E90 differentially regulate kinetics of VSD I transitions and current activation. (A,K) Schematic of VSD I in activated and resting states, showing the loss of ionic interactions upon mutation of E87A or E90A. **(B-G)** In Cav1.1e E87A right-shifted voltage-dependence of activation without affecting kinetics (wildtype (red), E87A (lime)). **(L-Q)** The E90A mutation accelerated kinetics >4-fold and right-shifted voltage-dependence of activation (wildtype (red), E87A (purple)). **(B,L)** Normalized representative currents show acceleration of activation in E90A **(L)** but not in E87A **(B)**. **(C,M)** Time to peak ($p=0.47$ in **C**, $p=0.00017$ in **M**); **(D,N)** current-voltage relationship; **(E,O)** maximum current density ($p=0.08$ in **E**, $p=0.04$ in **O**); **(F,P)** voltage-dependence of activation; **(G,Q)** voltage at half-maximal activation ($V_{1/2}$) ($p=0.000014$ in **G**, $p=0.008$ in **Q**). Mean \pm SEM; p -values calculated with student t-test. **(H-J)** The tICA free energy surface and schematic 1D representation of E87A show four macrostates corresponding to resting states 1, 2, 3 and the activated state with energy barriers similar to wildtype (gray) and transition kinetics in the higher microsecond timescale. **(R-T)** E90A shows three macrostates corresponding to the resting states 1 and 3 and the activated state, reduced energy barriers, and transition kinetics in the low microsecond timescale.

Figure 5-figure supplement 1: Deactivation kinetics are fast in Cav1.1e WT and in slowly (E87A) and fast-activating (E90A) VSD I mutants. (A) Voltage-clamp protocol used to examine deactivation kinetics (top) and representative current traces (bottom). Upon repolarization from +60 mV to varying negative potentials (at 10 mV increments), activated channels conduct a transient inward

calcium current (downward spike) before they deactivate and close the channel pore. The decay of this so-called *tail current* was fitted with a mono-exponential function to determine the time constants of deactivation. **(B)** The time constants of deactivation are equally fast in Ca_v1.1e WT, E90A, and E87A (in contrast to their distinct activation kinetics; cf. Figure 5 – figure supplement 6). At -20 mV significant kinetic differences start to occur, because at such weak repolarization part of the channels fail to deactivate and thus contaminate the tail current with a slowly inactivating current component ($p=0.019$; two-way repeated measure ANOVA and Holm-Sidak posthoc test). **(C)** Simplified model explaining slow activation and fast deactivation of the channel. We assume that at least two VSDs need to be in the up-state for the channel gate to open (at +60 mV). In response to the depolarizing voltage step the slow VSD (orange; VSD I in CaV1.1) will be rate-limiting and thus endow the channel with slow activation kinetics. On repolarization, the rapid downward movement of another VSD (green) will close the channel gate with fast deactivation kinetics, thus masking the continuing downward movement of the slow VSD.

Additional files

Supplementary file 1

Mean values and confidence intervals for probabilities and mean first passage times calculated from the Bayesian MSM, the confidence intervals are calculated at a confidence level of 95%.

Supplementary file 2

Current properties of E87A/E90A, E87A, E90A and WT controls.

Supplementary file 3

Linear Interaction Energy (LIE) calculations with the programm *cptraj* for the two VSDs and the mutants to calculate the electrostatic interactions of the S4 helix with all other parts of the voltage sensor.

Supplementary file 4

Summary table of the modelled loops in the voltage sensors with ab-initio Rosetta (Robetta).

Supplementary file 5

Primers used for site-directed mutagenesis.

Supplementary file 6

Input Scripts.

Video legends:

Video 1: Movement of wildtype Ca_v1.1 VSD I upon activation and deactivation, highlighting the ion-pair interactions formed between the S4 gating charges (blue) and relevant counter-charges (red) in the S2 and S3 helices.

Video 2: Movement of the E87A/E90A double-mutant of Ca_v1.1 VSD I upon activation and deactivation, highlighting the ion-pair interactions formed between the S4 gating charges (blue) and relevant counter-charges (red) in the S2 and S3 helices.

Video 3: Movement of the E87A mutant of Ca_v1.1 VSD I upon activation and deactivation, highlighting the ion-pair interactions formed between the S4 gating charges (blue) and relevant counter-charges (red) in the S2 and S3 helices.

Video 4: Movement of the E90A mutant of Ca_v1.1 VSD I upon activation and deactivation, highlighting the ion-pair interactions formed between the S4 gating charges (blue) and relevant counter-charges (red) in the S2 and S3 helices.

References for Supplementary file 1

Ahern CA, Payandeh J, Bosmans F, Chanda B. 2016. The hitchhiker's guide to the voltage-gated sodium channel galaxy. *J Gen Physiol* **147**:1–24. doi:10.1085/jgp.201511492

Bender BJ, Cisneros A, Duran AM, Finn JA, Fu D, Lokits AD, Mueller BK, Sangha AK, Sauer MF, Sevy AM, Sliwoski G, Sheehan JH, DiMaio F, Meiler J, Moretti R. 2016. Protocols for molecular modeling with Rosetta3 and RosettaScripts. *Biochemistry* **55**:4748–4763. doi:10.1021/acs.biochem.6b00444

Canutescu AA, Dunbrack RL. 2003. Cyclic coordinate descent: A robotics algorithm for protein loop closure. *Protein Sci* **12**:963–972. doi:10.1110/ps.0242703

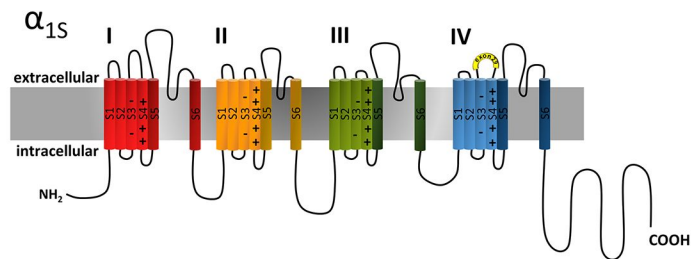
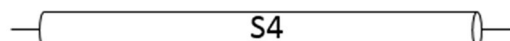
Case DA, Ben-Shalom IY, Brozell SR, Cerutti DS, Cheatham TEI, Cruzeiro VWD, Darden TA, Duke RE, Ghoreishi D, Gilson MK, Gohlke H, Goetz AW, Greene D, Harris R, Homeyer N, Izadi S, Kovalenko

- 940 A, Kurtzman T, Lee TS, LeGra S, York DM, Kollman PA. 2018. AMBER 2018. *Univ California, San*
941 *Fr.*
- 942 Catterall WA, Lenaues MJ, El-Din TMG. 2020. Structure and pharmacology of voltage-gated sodium
943 and calcium channels. *Annu Rev Pharmacol Toxicol* **60**:1–22. doi:10.1146/annurev-pharmtox-
944 010818-021757
- 945 Catterall WA, Wisedchaisri G, Zheng N. 2017. The chemical basis for electrical signaling. *Nat Chem*
946 *Biol* **13**:455–463. doi:10.1038/nchembio.2353
- 947 Chodera JD, Noé F. 2014. Markov state models of biomolecular conformational dynamics. *Curr Opin*
948 *Struct Biol* **25**:135–44. doi:10.1016/j.sbi.2014.04.002
- 949 Dickson CJ, Madej BD, Skjevik AA, Betz RM, Teigen K, Gould IR, Walker RC. 2014. Lipid14: The Amber
950 lipid force field. *J Chem Theory Comput* **10**:865–879. doi:10.1021/ct4010307
- 951 El Ghaleb Y, Campiglio M, Flucher BE. 2019. Correcting the R165K substitution in the first voltage-
952 sensor of CaV1.1 right-shifts the voltage-dependence of skeletal muscle calcium channel
953 activation. *Channels (Austin)* **13**:62–71. doi:10.1080/19336950.2019.1568825
- 954 Flucher BE. 2020. Skeletal muscle Ca V 1 . 1 channelopathies 739–754.
- 955 Flucher BE. 2016. Specific contributions of the four voltage-sensing domains in L-type calcium
956 channels to gating and modulation. *J Gen Physiol* **148**:91–95. doi:10.1085/jgp.201611663
- 957 Flucher BE, Andrews SB, Daniels MP. 1994. Molecular organization of transverse tubule/sarcoplasmic
958 reticulum junctions during development of excitation-contraction coupling in skeletal muscle.
959 *Mol Biol Cell* **5**:1105–1118. doi:10.1091/mbc.5.10.1105
- 960 Jensen M, Jogini V, Borhani DW, Leffler AE, Dror RO, Shaw DE. 2012. Mechanism of voltage gating in
961 potassium channels. *Science (80-)* **336**:229–233. doi:10.1126/science.1216533
- 962 Jo S, Lim JB, Klauda JB, Im W. 2009. CHARMM-GUI membrane builder for mixed bilayers and its
963 application to yeast membranes. *Biophys J* **97**:50–58. doi:10.1016/j.bpj.2009.04.013
- 964 Laidler KJ, King MC. 1983. The development of transition-state theory. *J Phys Chem* **87**:2657–2664.
965 doi:10.1021/j100238a002
- 966 Lenaues MJ, Gamal El-Din TM, Ing C, Ramanadane K, Pomès R, Zheng N, Catterall WA. 2017.
967 Structures of closed and open states of a voltage-gated sodium channel. *Proc Natl Acad Sci*
968 **114**:E3051–E3060. doi:10.1073/pnas.1700761114

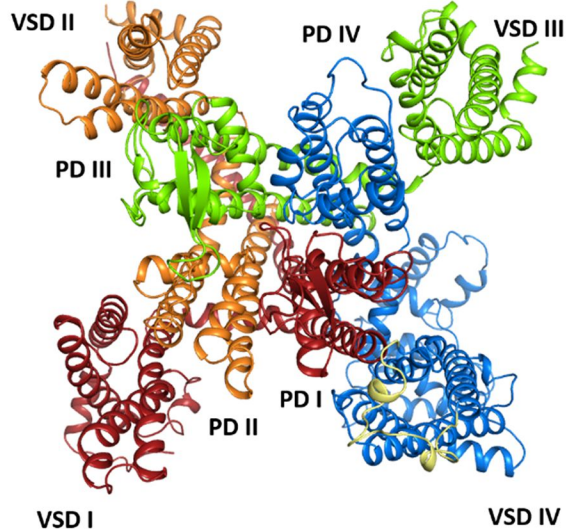
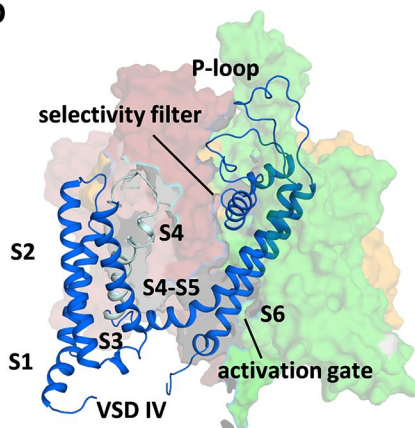
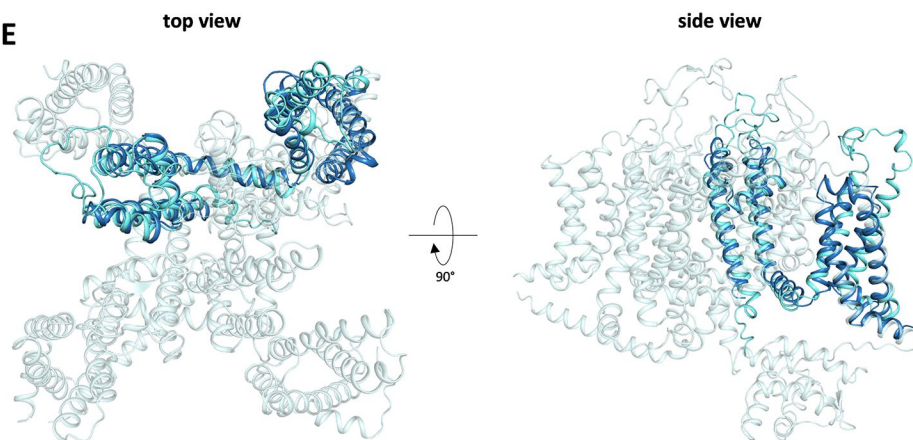
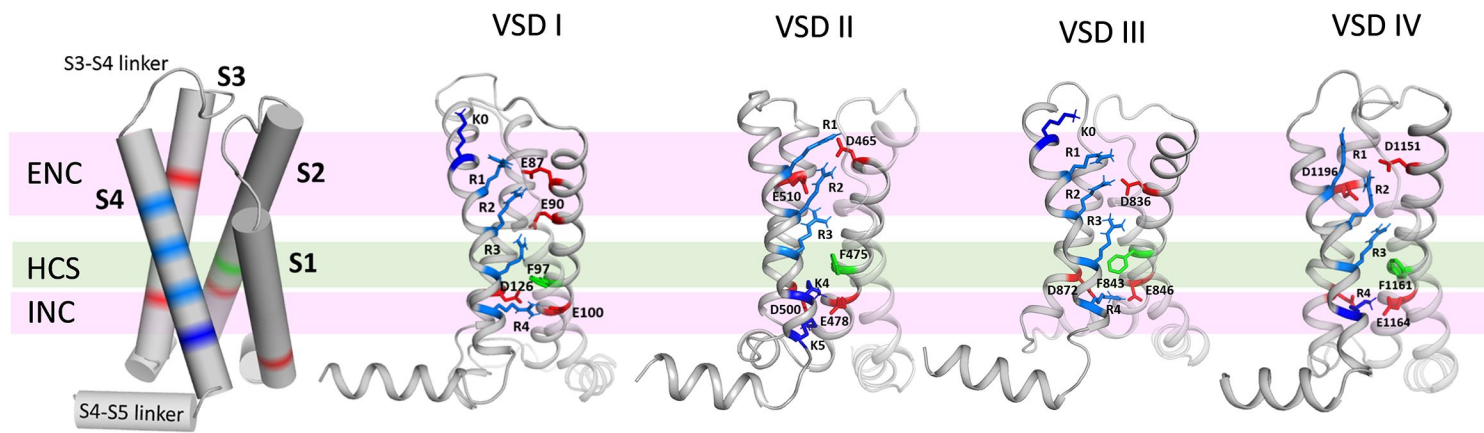
- 969 Likas A, Vlassis N, J. Verbeek J. 2003. The global k-means clustering algorithm. *Pattern Recognit*
970 **36**:451–461. doi:10.1016/S0031-3203(02)00060-2
- 971 Nakai J, Adams BA, Imoto K, Beam KG. 1994. Critical roles of the S3 segment and S3-S4 linker of
972 repeat I in activation of L-type calcium channels. *Proc Natl Acad Sci* **91**:1014–1018.
- 973 Pan X, Li Z, Zhou Q, Shen H, Wu K, Huang X, Chen J, Zhang J, Zhu X, Lei J, Xiong W, Gong H, Xiao B, Yan
974 N. 2018. Structure of the human voltage-gated sodium channel Nav1.4 in complex with β 1.
975 *Science (80-)* **362**. doi:10.1126/science.aau2486
- 976 Pantazis A, Savalli N, Sigg D, Neely A, Olcese R. 2014. Functional heterogeneity of the four voltage
977 sensors of a human L-type calcium channel. *Proc Natl Acad Sci* **111**:18381–18386.
978 doi:10.1073/pnas.1411127112
- 979 Payandeh J, Scheuer T, Zheng N, Catterall WA. 2011. The crystal structure of a voltage-gated sodium
980 channel. *Nature* **475**:353–358. doi:10.1038/nature10238
- 981 Pérez-Hernández G, Noé F. 2016. Hierarchical time-lagged independent component analysis:
982 Computing slow modes and reaction coordinates for large molecular systems. *J Chem Theory*
983 *Comput* **12**:6118–6129. doi:10.1021/acs.jctc.6b00738
- 984 Powell JA, Petherbridge L, Flucher BE. 1996. Formation of triads without the dihydropyridine
985 receptor subunits in cell lines from dysgenic skeletal muscle. *J Cell Biol* **134**:375–387.
986 doi:10.1083/jcb.134.2.375
- 987 Röblitz S, Weber M. 2013. Fuzzy spectral clustering by PCCA+: application to Markov state models
988 and data classification. *Adv Data Anal Classif* **7**:147–179. doi:10.1007/s11634-013-0134-6
- 989 Roe DR, Cheatham TE. 2013. PTRAJ and CPPTRAJ: Software for processing and analysis of molecular
990 dynamics trajectory data. *J Chem Theory Comput* **9**:3084–95. doi:10.1021/ct400341p
- 991 Rohl CA, Strauss CEM, Misura KMS, Baker D. 2004. Protein structure prediction using Rosetta.
992 *Methods Enzymol* **383**:66–93. doi:10.1016/S0076-6879(04)83004-0
- 993 Scherer MK, Trendelkamp-Schroer B, Paul F, Pérez-Hernández G, Hoffmann M, Plattner N, Wehmeyer
994 C, Prinz J-H, Noé F. 2015. PyEMMA 2: A software package for estimation, validation, and
995 analysis of Markov models. *J Chem Theory Comput* **11**:5525–42. doi:10.1021/acs.jctc.5b00743
- 996 Tanabe T, Beam KG, Powell JA, Numa S. 1988. Restoration of excitation-contraction coupling and
997 slow calcium current in dysgenic muscle by dihydropyridine receptor complementary DNA.
998 *Nature* **336**:134–9. doi:10.1038/336134a0

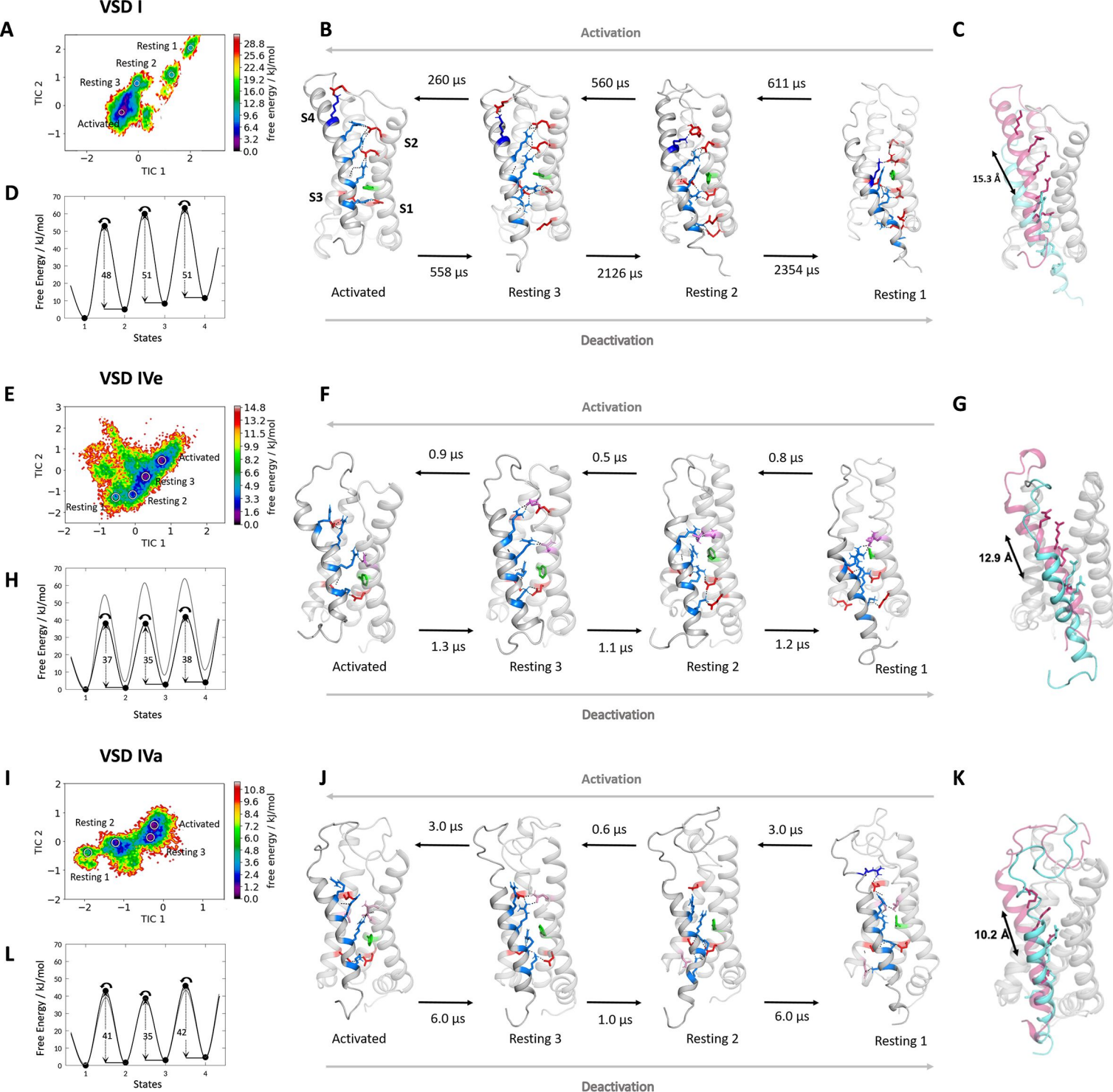
- 999 Tao X, Lee A, Limapichat W, Dougherty DA, MacKinnon R. 2010. A gating charge transfer center in
1000 voltage sensors. *Science (80-)* **328**:67–73. doi:10.1126/science.1185954
- 1001 Tuluc P, Benedetti B, Coste De Bagneaux P, Grabner M, Flucher BE. 2016a. Two distinct voltage-
1002 sensing domains control voltage sensitivity and kinetics of current activation in CaV1.1 calcium
1003 channels. *J Gen Physiol* **147**:437–449. doi:10.1085/jgp.201611568
- 1004 Tuluc P, Molenda N, Schlick B, Obermair GJ, Flucher BE, Jurkat-Rott K. 2009. A Cav1.1 Ca²⁺ channel
1005 splice variant with high conductance and voltage-sensitivity alters EC coupling in developing
1006 skeletal muscle. *Biophys J* **96**:35–44. doi:10.1016/j.bpj.2008.09.027
- 1007 Tuluc P, Yarov-Yarovoy V, Benedetti B, Flucher BE. 2016b. Molecular interactions in the voltage
1008 sensor controlling gating properties of CaV calcium channels. *Structure* **24**:261–271.
1009 doi:10.1016/j.str.2015.11.011
- 1010 Wang C, Bradley P, Baker D. 2007. Protein-protein docking with backbone flexibility. *J Mol Biol*
1011 **373**:503–519. doi:10.1016/j.jmb.2007.07.050
- 1012 Wisedchaisri G, Tonggu L, Gamal El-Din TM, McCord E, Zheng N, Catterall WA. 2021. Structural basis
1013 for high-affinity trapping of the Nav1.7 channel in its resting state by tarantula toxin. *Mol Cell*
1014 **81**:38-48.e4. doi:10.1016/j.molcel.2020.10.039
- 1015 Wisedchaisri G, Tonggu L, McCord E, Gamal El-Din TM, Wang L, Zheng N, Catterall WA. 2019. Resting-
1016 state structure and gating mechanism of a voltage-gated sodium channel. *Cell* **178**:993-
1017 1003.e12. doi:10.1016/j.cell.2019.06.031
- 1018 Wu H, Noé F. 2020. Variational approach for learning Markov processes from time series data. *J*
1019 *Nonlinear Sci* **30**:23–66. doi:10.1007/s00332-019-09567-y
- 1020 Wu J, Yan Z, Li Z, Qian X, Lu S, Dong M, Zhou Q, Yan N. 2016. Structure of the voltage-gated calcium
1021 channel Cav1.1 at 3.6 Å resolution. *Nature* **537**:191–196. doi:10.1038/nature19321
- 1022 Wu J, Yan Z, Li Z, Yan C, Lu S, Dong M, Yan N. 2015. Structure of the voltage-gated calcium channel
1023 Cav1.1 complex. *Science (80-)* **350**:aad2395-1–9. doi:10.1126/science.aad2395
- 1024 Xu H, Li T, Rohou A, Arthur CP, Tzakoniati F, Wong E, Estevez A, Kugel C, Franke Y, Chen J, Ciferri C,
1025 Hackos DH, Koth CM, Payandeh J. 2019. Structural basis of Nav1.7 inhibition by a gating-
1026 modifier spider toxin. *Cell* **176**:702–715. doi:10.1016/j.cell.2018.12.018
- 1027 Yan Z, Zhou Q, Wang L, Wu J, Zhao Y, Huang G, Peng W, Shen H, Lei J, Yan N. 2017. Structure of the
1028 Nav1.4-β1 Complex from Electric Eel. *Cell* **170**:470-475.e11. doi:10.1016/j.cell.2017.06.039

- 1029 Yarov-Yarovoy V, DeCaen PG, Westenbroek RE, Pan C-Y, Scheuer T, Baker D, Catterall WA. 2012.
1030 Structural basis for gating charge movement in the voltage sensor of a sodium channel. *Proc*
1031 *Natl Acad Sci U S A* **109**:E93-102. doi:10.1073/pnas.1118434109
- 1032 Zhang X, Ren W, DeCaen P, Yan C, Tao X, Tang L, Hasegawa K, Kumasaka T, He J, Wang JJ, Clapham
1033 DE, Yan N, Hasegawa K, Kumasaka T, He J, Wang JJ, Clapham DE, Yan N. 2012. Crystal structure
1034 of an orthologue of the NaChBac voltage-gated sodium channel. *Nature* **486**:130–134.
1035 doi:10.1038/nature11054
- 1036 Zhao Y, Huang G, Wu J, Wu Q, Gao S, Yan Z, Lei J, Yan N. 2019. Molecular basis for ligand modulation
1037 of a mammalian voltage-gated Ca²⁺ channel. *Cell* **177**:1495–1506.
1038 doi:10.1016/j.cell.2019.04.043
- 1039

A**C**

NavAB S4	S S G F E I L R V L R V L R L F R L V T A
Cav1.1 IS4	G L D V K A L R A F R V L R P L R L V S G
Cav1.1 IIS4	P L G I S V L R C I R L L R L F K I T K Y
Cav1.1 IIIS4	I S V V K I L R V L R V L R P L R A I N R
Cav1.1 IVS4	R I S S A F F R L F R V M R L V K L L N R
	R0 R1 R2 R3 R4 R5

B**D****E****F**



A

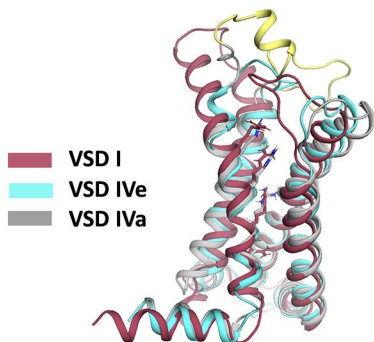
VSD I					
Simple	Gating Charge	Activated	Resting 3	Resting 2	Resting 1
K0	K162	E76	E76		
R1	R165	E87	E87	E90	D126
R2	R168	E87, E90	E90	D126	D126, E100
R3	R171	E90	E100, D126	D126, E100	E49
R4	R174	E100, D126	D126	E100, E49	

VSD IVa					
Simple	Gating Charge	Activated	Resting 3	Resting 2	Resting 1
R1	R1236				
R2	R1239	D1196			
R3	R1242			D1186	E1164, D1186
K4	R1245	D1186, E1164	D1186	E1121	E1121

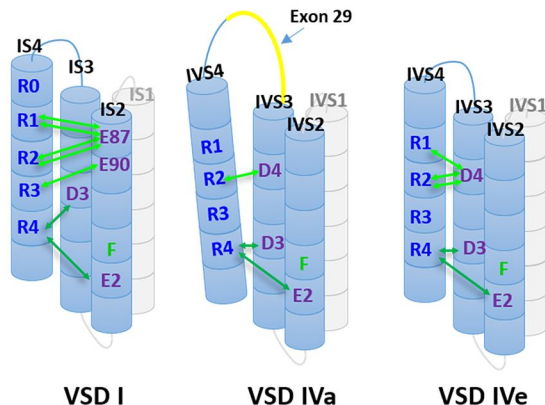
VSD IVe					
Simple	Gating Charge	Activated	Resting 3	Resting 2	Resting 1
R1	R1217	D1196			
R2	R1220	D1151, D1196			
R3	R1223		D1186	D1186	E1164, D1186
K4	K1226	D1186, E1164	D1186, E1164	E1121, E1164	E1121

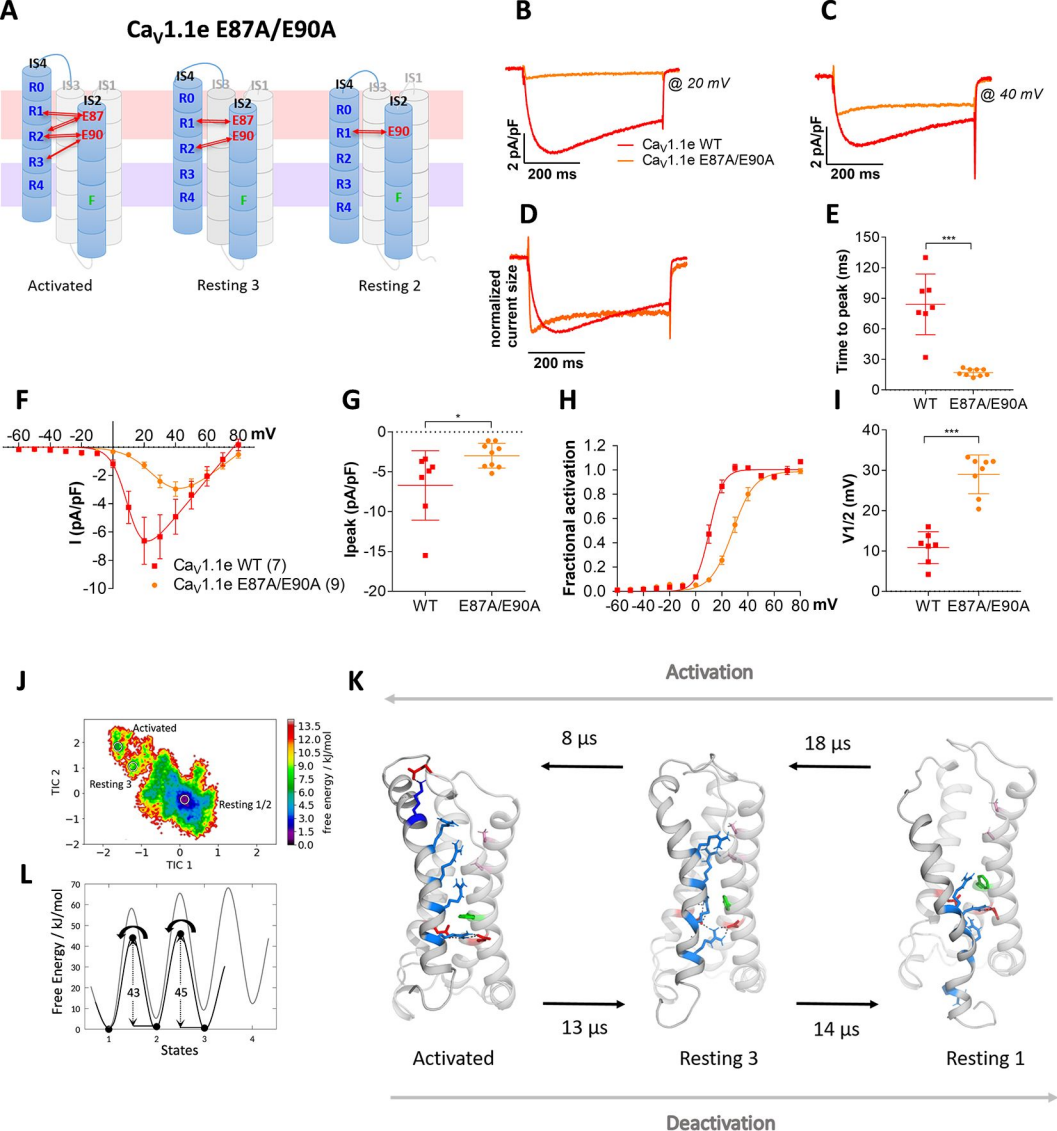
Ion-pairs in ENC
Ion-pairs in CTC

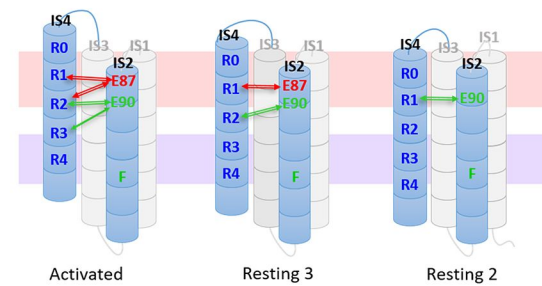
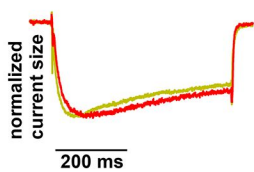
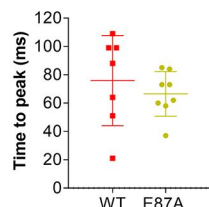
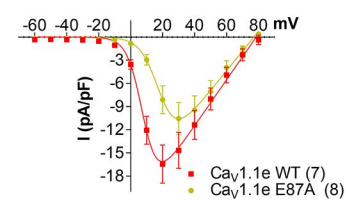
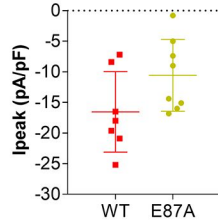
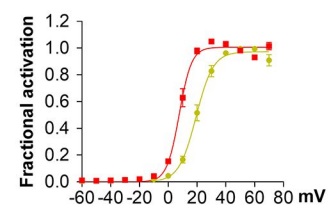
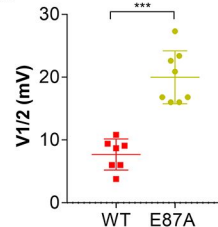
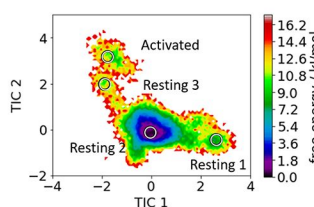
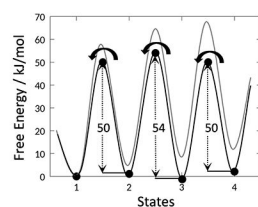
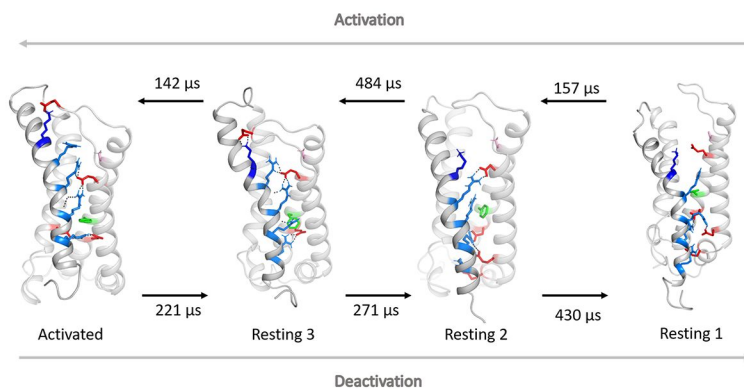
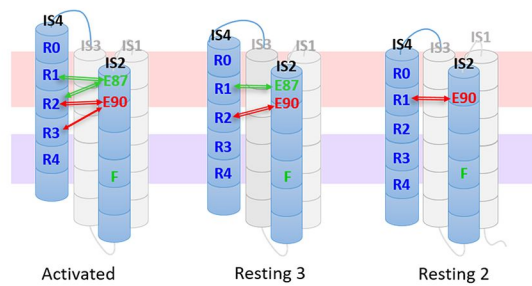
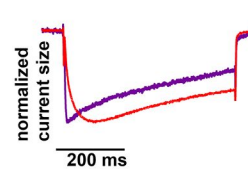
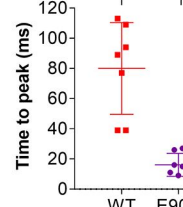
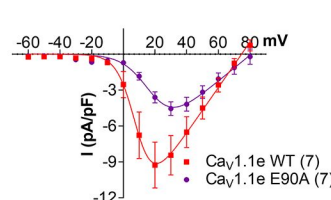
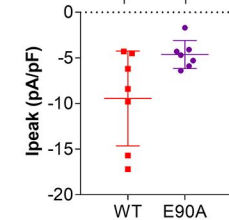
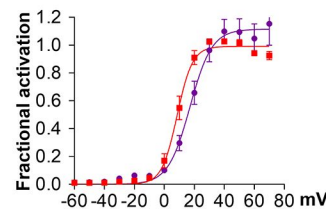
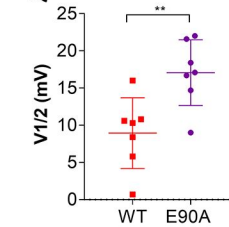
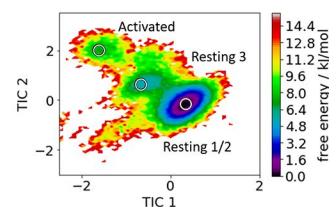
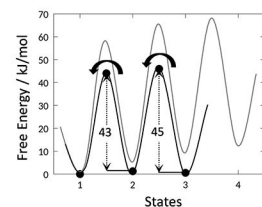
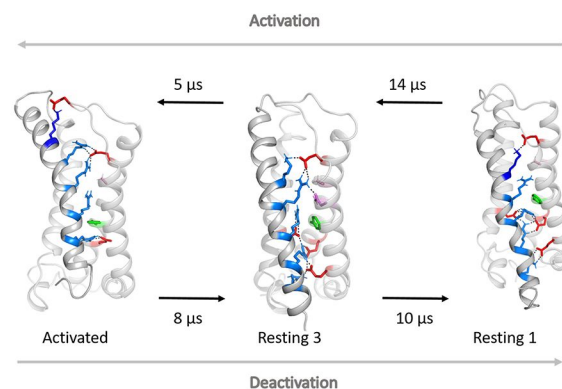
B

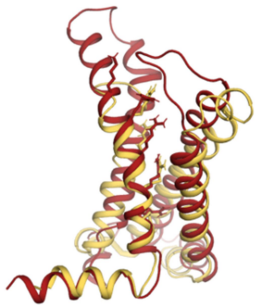


C

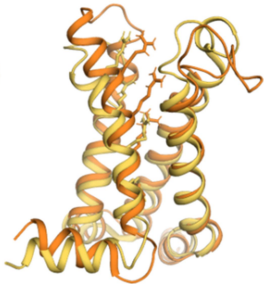




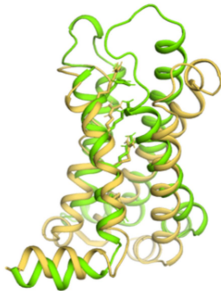
Ca_v1.1e E87A**B****C****D****E****F****G****H****J****I****Ca_v1.1e E90A****L****M****N****O****P****Q****R****T****S**



■ VSD I
■ Na_vAB



■ VSD II
■ Na_vAB



■ VSD III
■ Na_vAB

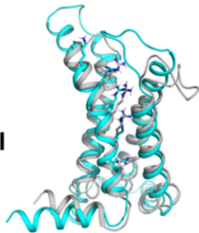


■ VSD IVe
■ Na_vAB

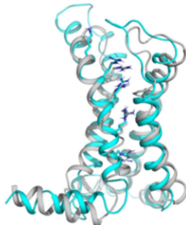


■ VSD IVa
■ Na_vAB

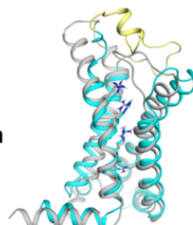
I vs II



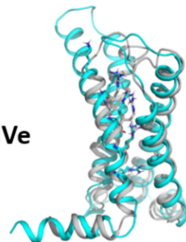
I vs III



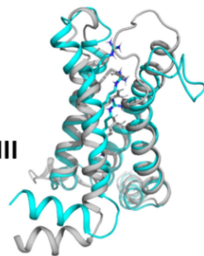
I vs IVa



I vs IVe



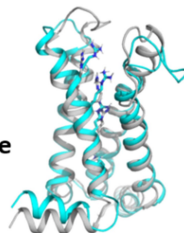
II vs III



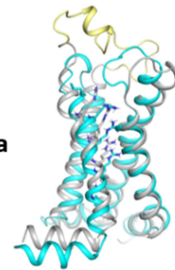
II vs IVa



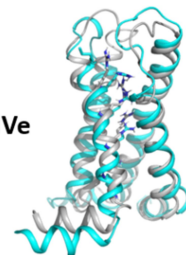
II vs IVe



III vs IVa



III vs IVe

Ca_v1.1e (RMSD, Å)

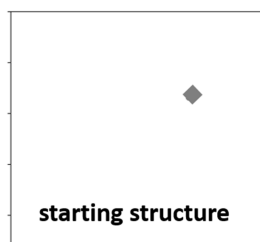
VSD	I	II	III	IV
I		2.9	2.8	2.60
II	1.20		3.1	1.8
III	1.10	1.20		2.9
IV	1.30	1.18	1.20	

S1 ~S4 w/o loops

IV+E29
2.8
3.1
3.9

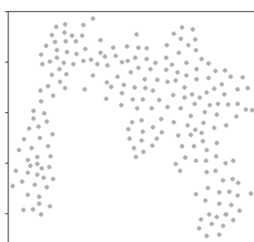
S4 only

IV+E29	0.9	0.9	1.4	
--------	-----	-----	-----	--



Umbrella sampling

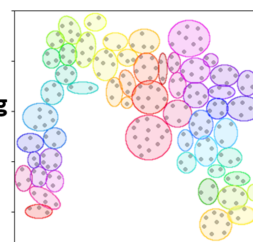
1



geometric clustering

2

Generation of starting structures for MD simulations



tICA - coordinate transformation

3

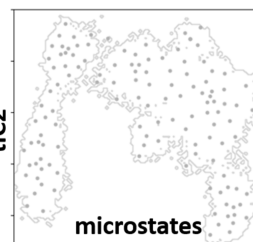
MD simulations



kinetic clustering to define microstates

4

k-means clustering

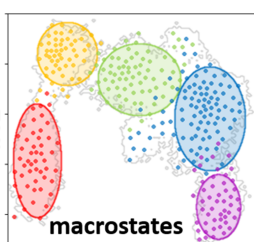


spectral clustering

PCCA+ clustering

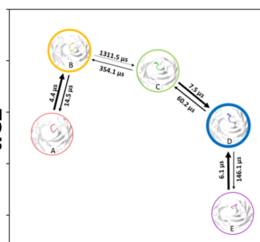
5

Coarse-graining microstates to macrostates



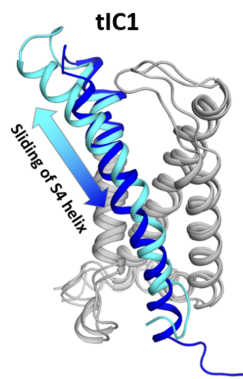
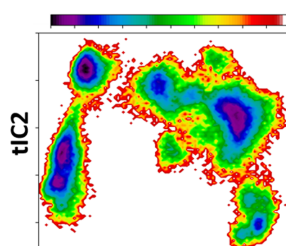
Markov-state model

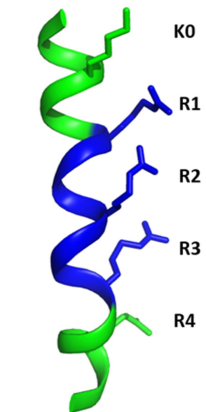
6



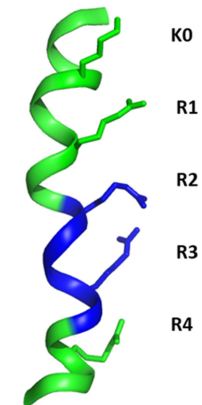
reconstruction of kinetics and thermodynamics

free energy surface





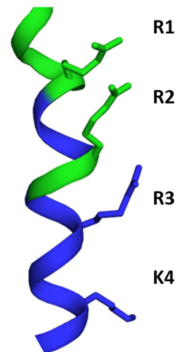


VSD I
activated state

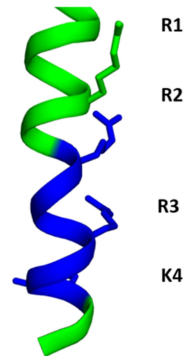


VSD I
resting state 1

 **3₁₀-Helix**
 **α-Helix**

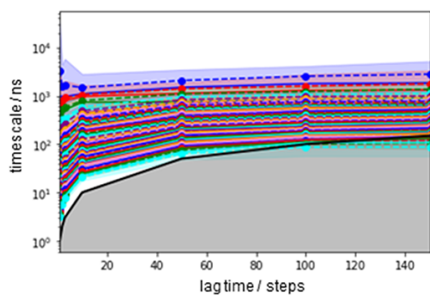


VSD IV
activated state

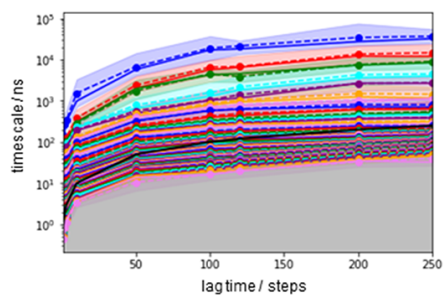


VSD IV
resting state 1

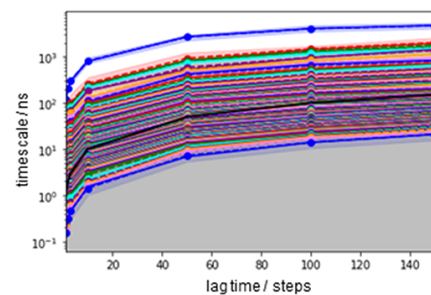
VSD I E87A/E90A



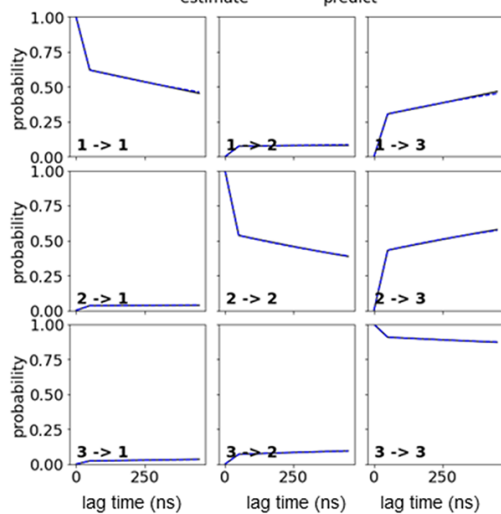
VSD I E87A



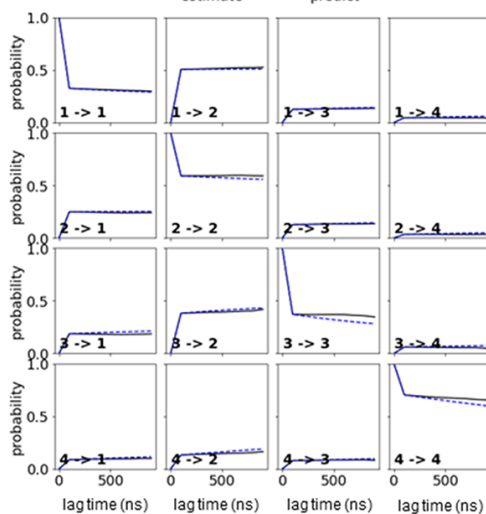
VSD I E90A



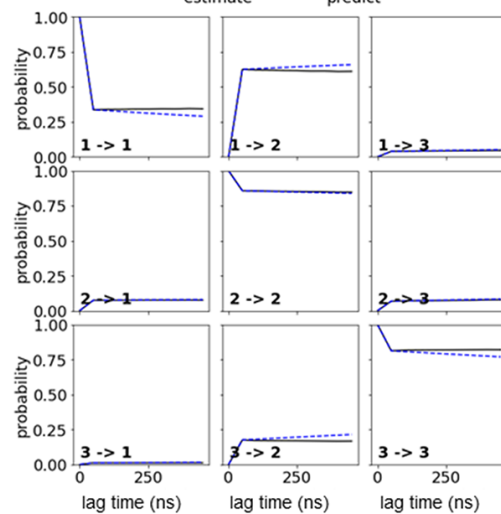
— estimate - - - predict



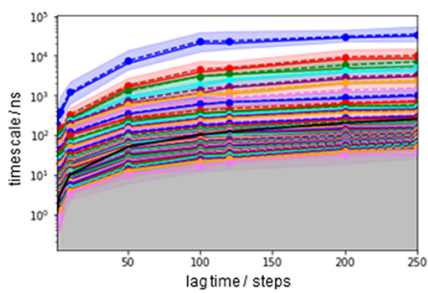
— estimate - - - predict



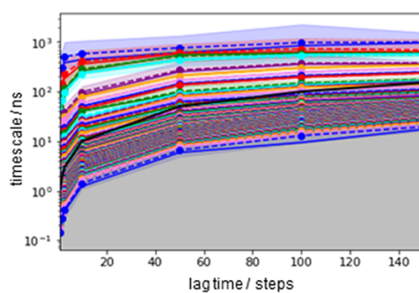
— estimate - - - predict



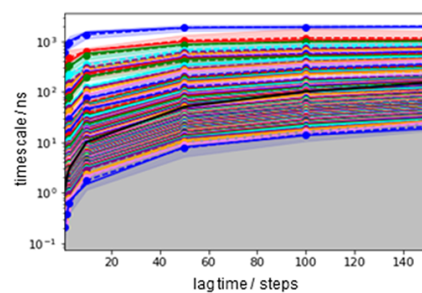
VSD I WT



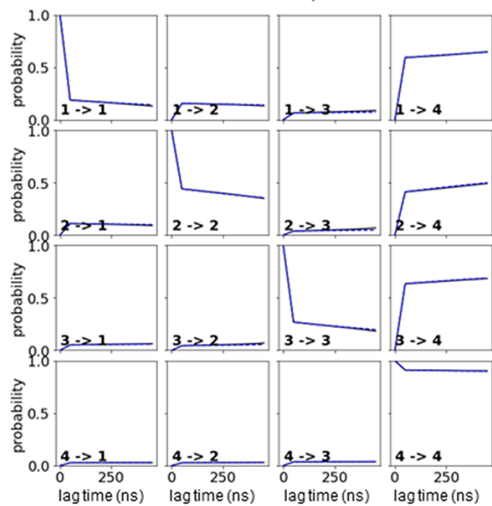
VSD I Ve



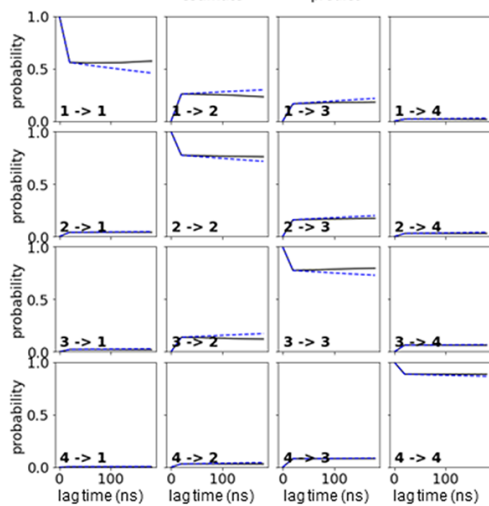
VSD IVa



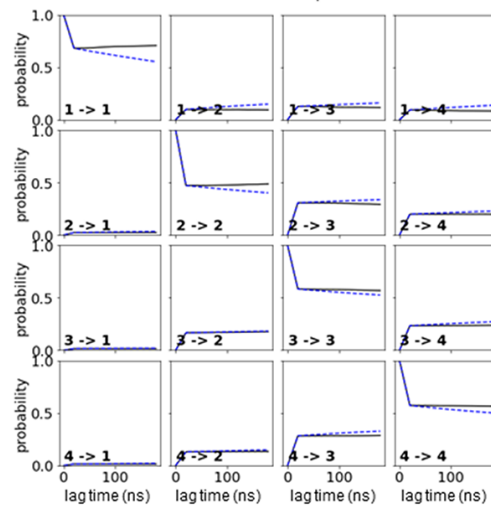
— estimate - - - predict

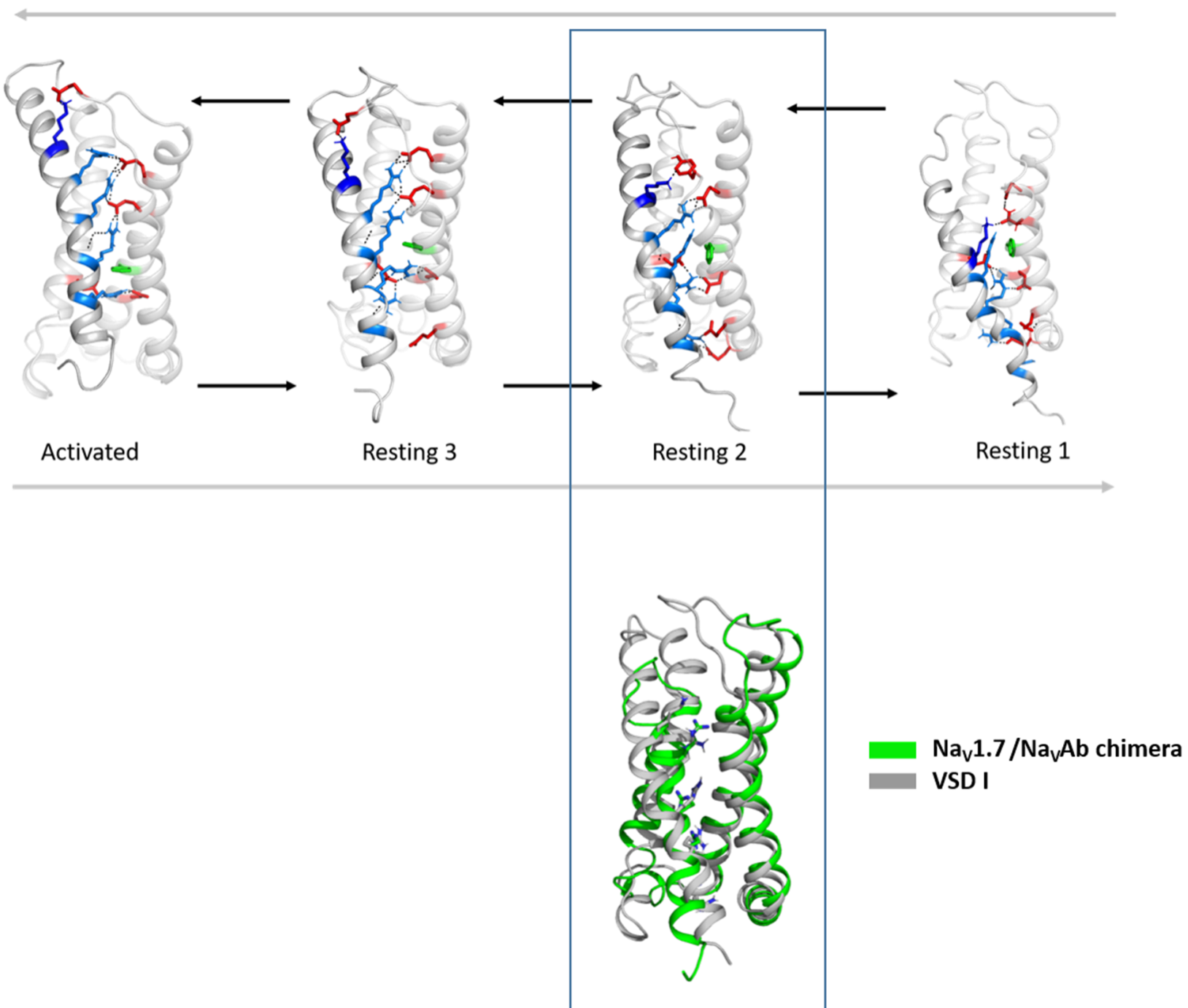


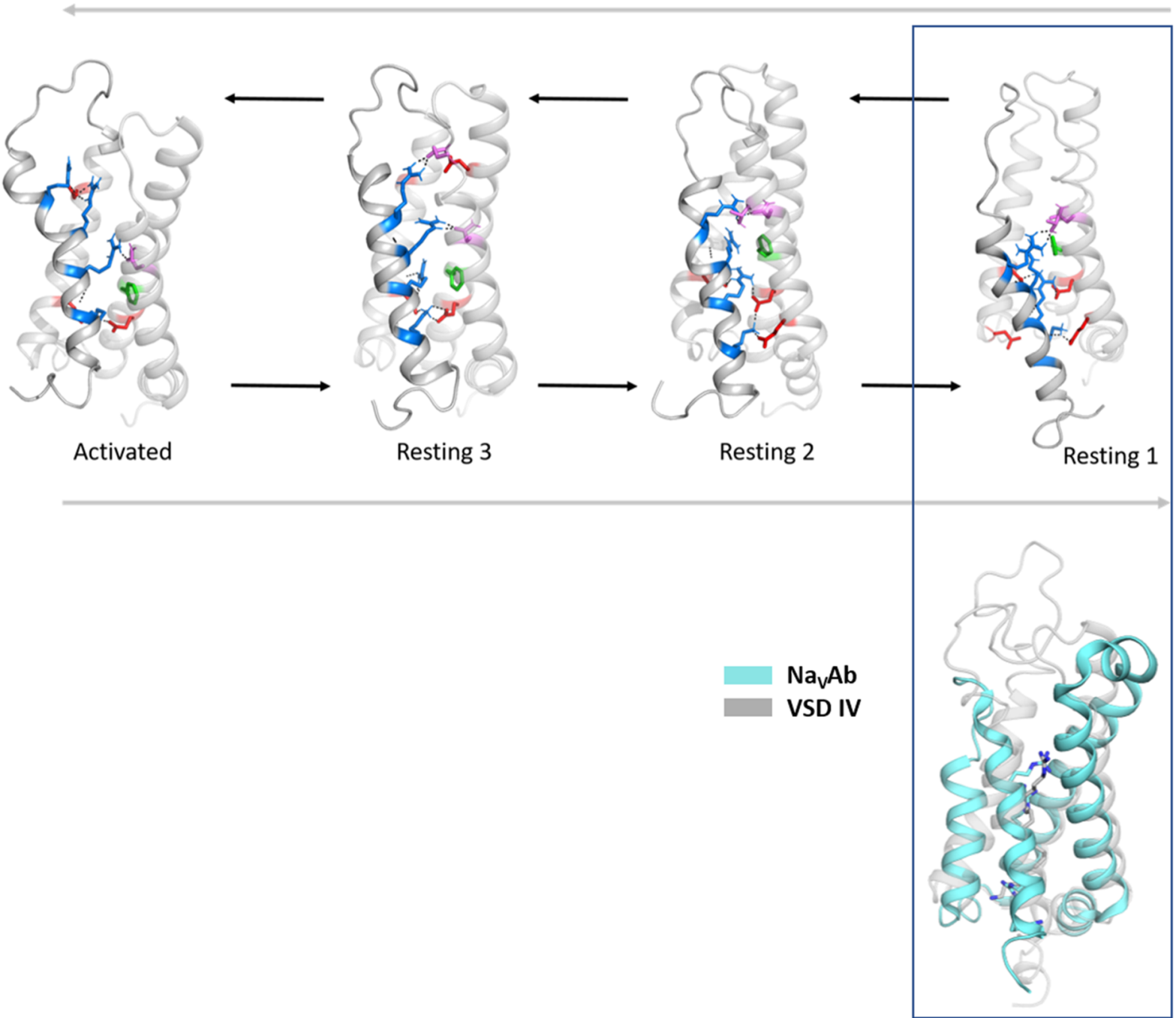
— estimate - - - predict



— estimate - - - predict







anti-GFP-Ca_v1.1

anti-RyR1

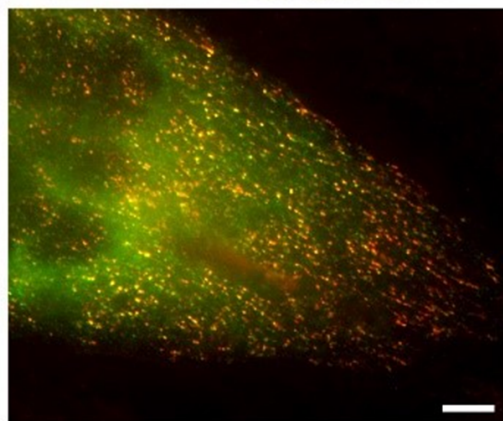
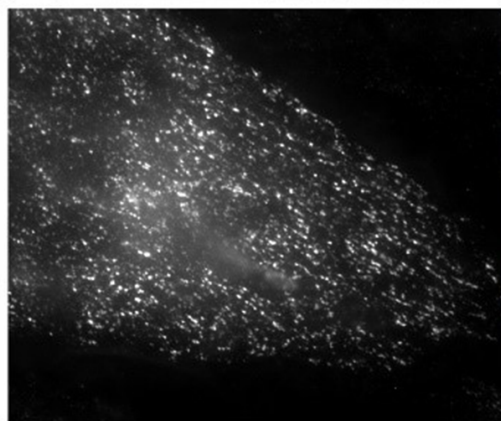
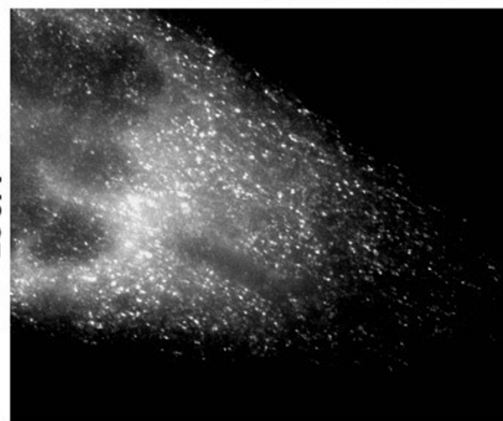
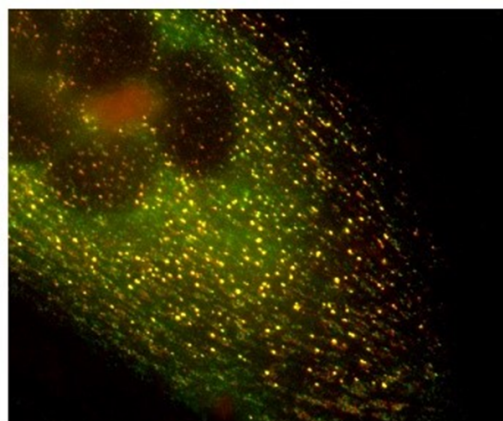
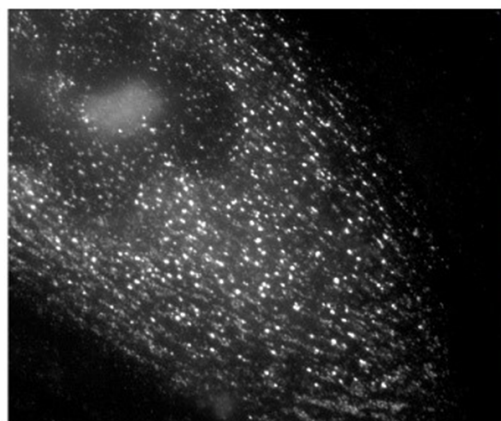
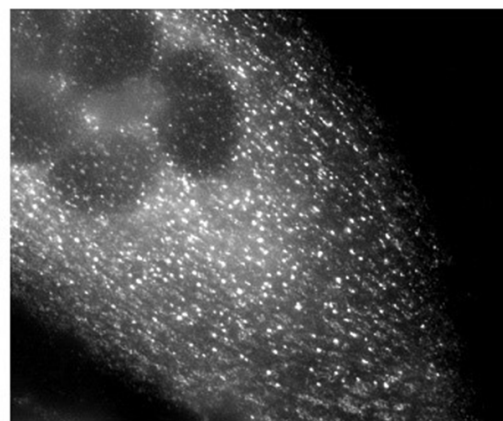
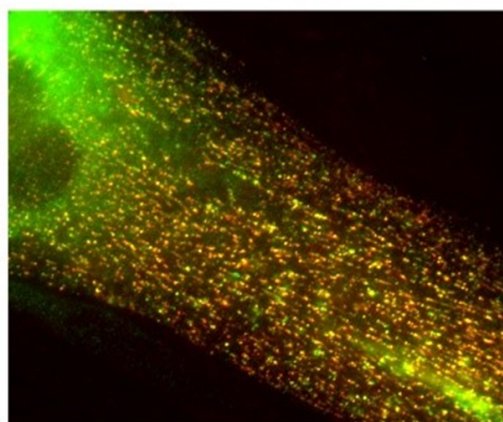
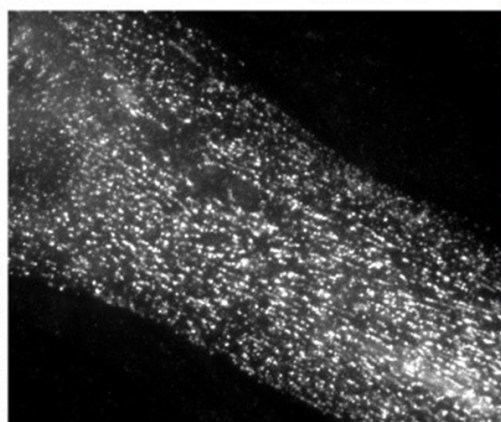
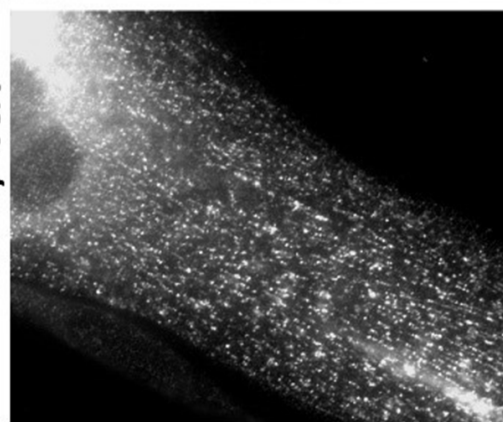
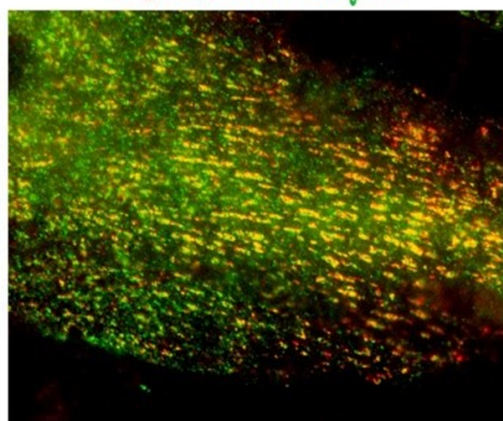
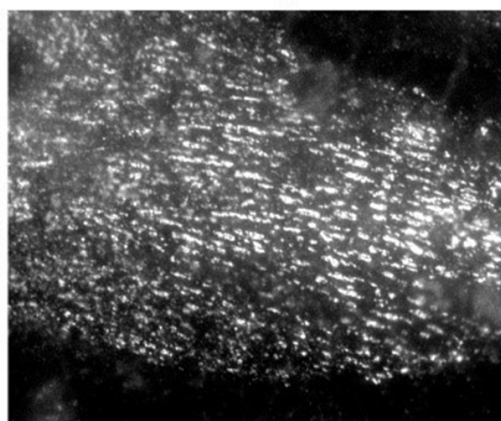
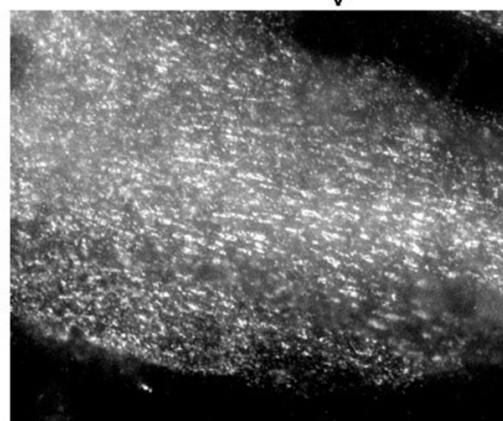
RyR1/GFP-Ca_v1.1

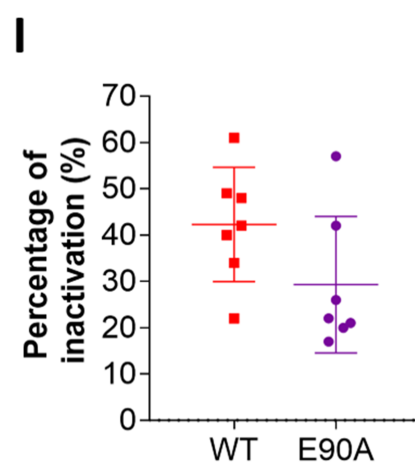
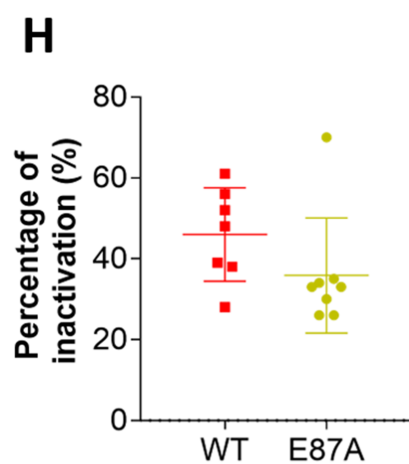
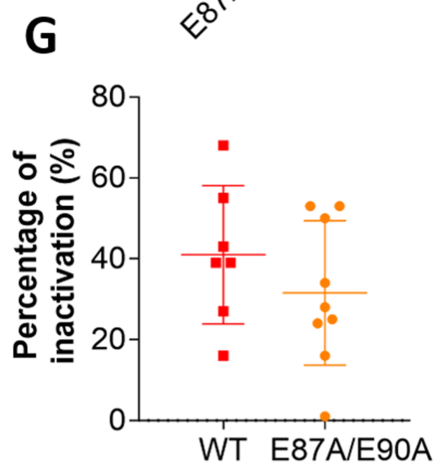
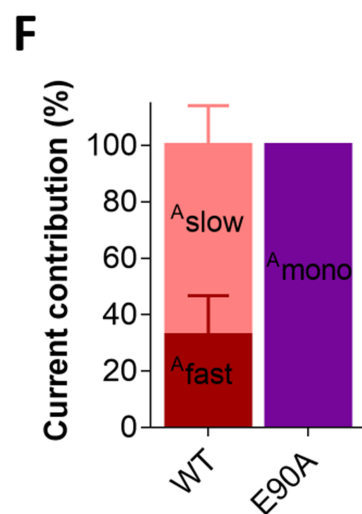
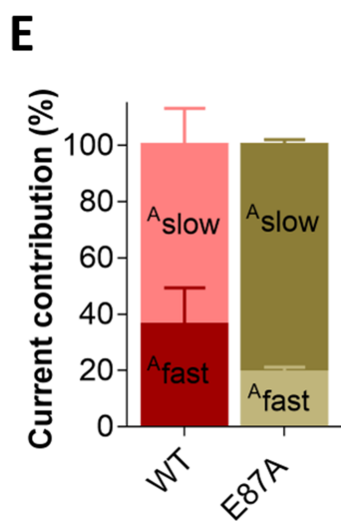
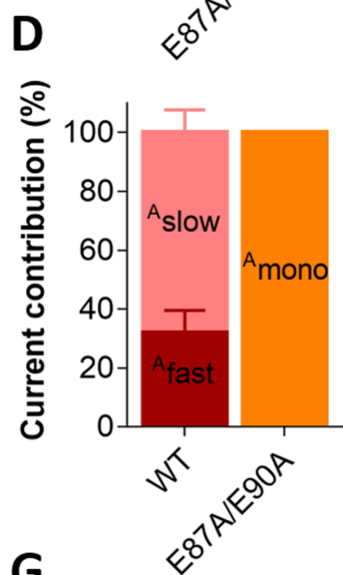
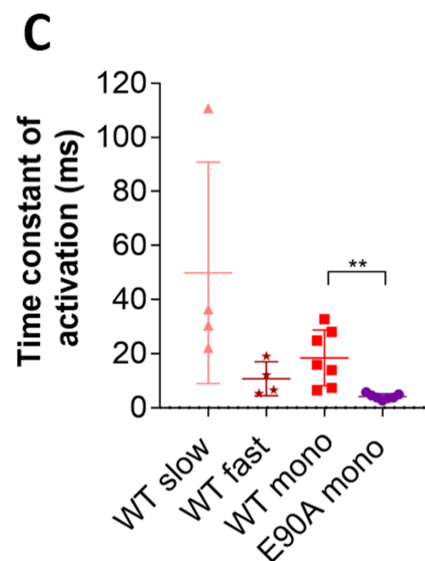
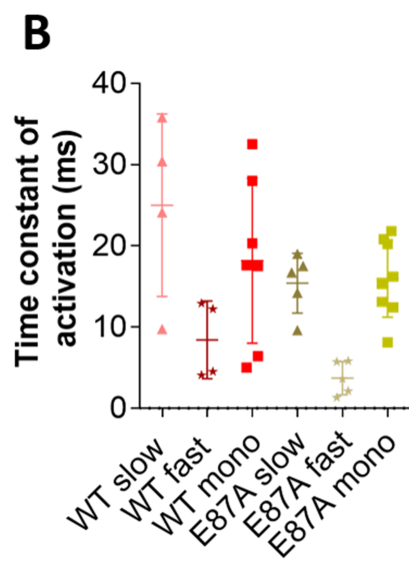
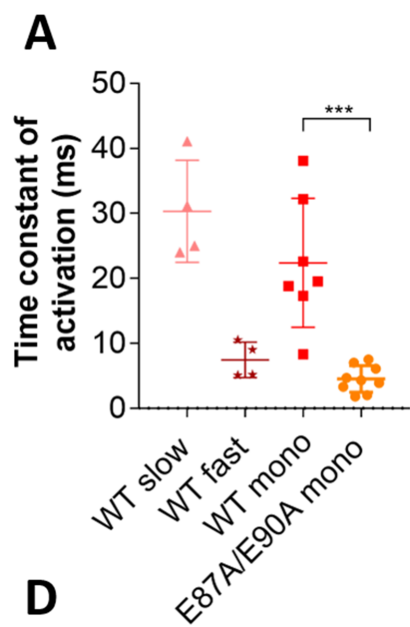
WT

E87A/E90A

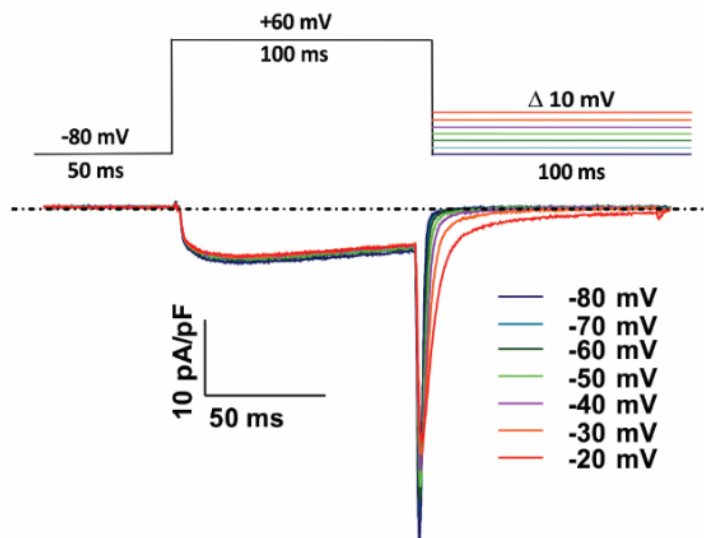
E87A

E90A

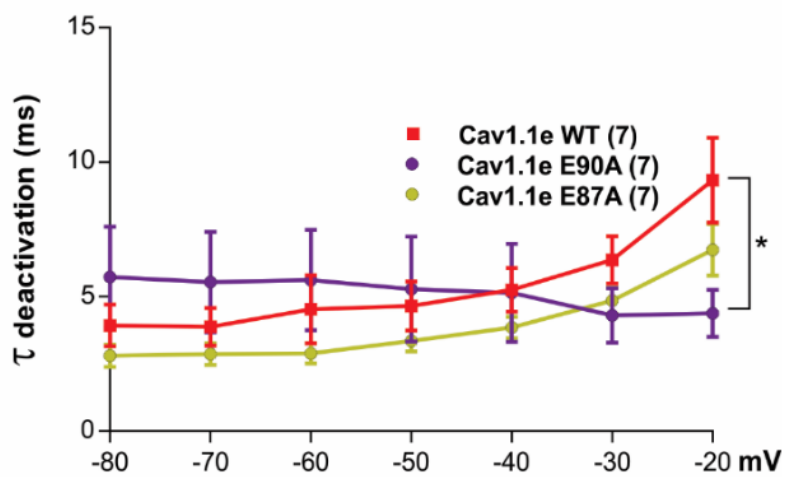




A



B



C

